



**HAL**  
open science

# Nonlinear wave attenuation in strongly-confined falling liquid films sheared by a laminar counter-current gas flow

Sophie Mergui, Gianluca Lavallo, Yiqin Li, Nicolas Grenier, Georg F. Dietze

► **To cite this version:**

Sophie Mergui, Gianluca Lavallo, Yiqin Li, Nicolas Grenier, Georg F. Dietze. Nonlinear wave attenuation in strongly-confined falling liquid films sheared by a laminar counter-current gas flow. *Journal of Fluid Mechanics*, 2023, 954, pp.A19. 10.1017/jfm.2022.967 . hal-03865136

**HAL Id: hal-03865136**

**<https://hal.science/hal-03865136v1>**

Submitted on 22 Nov 2022

**HAL** is a multi-disciplinary open access archive for the deposit and dissemination of scientific research documents, whether they are published or not. The documents may come from teaching and research institutions in France or abroad, or from public or private research centers.

L'archive ouverte pluridisciplinaire **HAL**, est destinée au dépôt et à la diffusion de documents scientifiques de niveau recherche, publiés ou non, émanant des établissements d'enseignement et de recherche français ou étrangers, des laboratoires publics ou privés.

## Nonlinear wave attenuation in strongly-confined falling liquid films sheared by a laminar counter-current gas flow

|                               |  |
|-------------------------------|--|
| Journal:                      | <i>Journal of Fluid Mechanics</i>  |
| Manuscript ID                 | JFM-22-0678.R1   |
| Manuscript Type:              | JFM Papers   |
| Date Submitted by the Author: | n/a  |
| Complete List of Authors:     | Mergui, Sophie; Fluides Automatique et Systemes Thermiques Lavallo, Gianluca; Mines Saint-Étienne, Centre SPIN - UMR CNRS 5307 LGF<br>Li, Yiqin; Fluides Automatique et Systemes Thermiques Grenier, Nicolas; Laboratoire d'Informatique pour la Mecanique et les Sciences de l'Ingenieur, Dietze, Georg; Fluides Automatique et Systemes Thermiques   |
| JFM Keywords:                 | Thin films < Interfacial Flows (free surface), Gas/liquid flows < Multiphase and Particle-laden Flows, Solitary waves < Waves/Free-surface Flows   |
| Abstract:                     | <p>Experiments are conducted in water films falling along the bottom wall of a weakly-inclined rectangular channel of height 5mm in the presence of a laminar counter-current air flow. Boundary conditions have been specifically designed to avoid flooding at the liquid outlet, thus allowing to focus on the wave dynamics in the core of the channel. Surface waves are excited via coherent inlet forcing before they come into contact with the air flow. The effect of the air flow on the height, shape, and speed of two-dimensional travelling nonlinear waves is investigated and contrasted with experiments of Kofman (Int. J. of Multiphase Flow, 2017, vol. 95) which were performed in a weakly-confined channel. We observe a striking difference between these two cases.</p> <p>In our strongly-confined configuration, a monotonic stabilizing effect or a non-monotonic trend (i.e. the wave height first increases and then diminishes upon increasing the gas flow rate) is observed, in contrast to the weakly-confined configuration where the gas flow is always destabilizing. This stabilizing effect implies the possibility of attenuating waves via the gas flow and it confirms recent numerical results obtained by Lavallo (J. Fluid Mech. Rapids, 2021, vol. 919) in a superconfined channel.</p> |

SCHOLARONE™  
Manuscripts

# Nonlinear wave attenuation in strongly-confined falling liquid films sheared by a laminar counter-current gas flow

Sophie Mergui<sup>1,2,†</sup>, Gianluca Lavallo<sup>3</sup>, Yiqin Li<sup>1</sup>, Nicolas Grenier<sup>4</sup>, and Georg F. Dietze<sup>1</sup>

<sup>1</sup>Université Paris-Saclay, CNRS, FAST, 91405 Orsay, France

<sup>2</sup>Sorbonne Université, UFR 919, 4 place Jussieu, F-75252 Paris Cedex 05, France

<sup>3</sup>Mines Saint-Etienne, Université Lyon, CNRS, UMR 5307 LGF, Centre SPIN, F-42023 Saint-Etienne, France

<sup>4</sup>Université Paris-Saclay, CNRS, LISN, 91405 Orsay, France

(Received xx; revised xx; accepted xx)

Experiments are conducted in water films falling along the bottom wall of a weakly-inclined rectangular channel of height 5 mm in the presence of a laminar counter-current air flow. Boundary conditions have been specifically designed to avoid flooding at the liquid outlet, thus allowing to focus on the wave dynamics in the core of the channel. Surface waves are excited via coherent inlet forcing before they come into contact with the air flow. The effect of the air flow on the height, shape, and speed of two-dimensional travelling nonlinear waves is investigated and contrasted with experiments of Kofman *et al.* (Int. J. of Multiphase Flow, 2017, vol. 95) which were performed in a weakly-confined channel. We observe a striking difference between these two cases. In our strongly-confined configuration, a monotonic stabilizing effect or a non-monotonic trend (i.e. the wave height first increases and then diminishes upon increasing the gas flow rate) is observed, in contrast to the weakly-confined configuration where the gas flow is always destabilizing. This stabilizing effect implies the possibility of attenuating waves via the gas flow and it confirms recent numerical results obtained by Lavallo *et al.* (J. Fluid Mech. Rapids, 2021, vol. 919) in a superconfined channel.

## 1. Introduction

We consider a falling liquid film in contact with a laminar counter-current gas flow within a narrow rectangular channel inclined at an angle  $\beta$  (figure 1). This configuration can be considered as a prototype for compact devices found in engineering applications, such as reflux condensers and distillation columns with structured packings (Valluri *et al.* 2005). It is well known that the interaction between the wavy film and the gas flow can promote flooding events leading to a deterioration in the process performance. Depending on the geometry and/or ratio of liquid and gas flow rates (or superficial velocities) we can observe film atomization (Zapke & Kröger 2000), wave or liquid flow reversal (Tseluiko & Kalliadasis 2011), or obstruction of the channel (Vlachos *et al.* 2001). In order to prevent or delay such events, it is crucial to characterize the dynamics of interfacial waves and in particular their linear and nonlinear responses to the gas flow.

Many theoretical and experimental works dedicated to the linear stability of falling films are reported in the literature since the seminal work of Kapitza (1948) on the

† Email address for correspondence: sophie.mergui@sorbonne-universite.fr

2

41 different wavy flow regimes. The linear stability analysis of a liquid film in a passive  
42 atmosphere was initiated by Benjamin (1957) and Yih (1963). They found that the film  
43 is unstable to long-wave disturbances when the Reynolds number is greater than  $5/6 \cot \beta$   
44 through an inertia-driven mechanism. This threshold for the so-called Kapitza instability  
45 was confirmed experimentally by Liu *et al.* (1993). Recent theoretical investigations  
46 (Lavalle *et al.* 2019) have shown that the impact of the gas phase on the linear stability  
47 threshold becomes non negligible in weakly inclined and/or strongly confined channels by  
48 causing a stabilizing effect and ultimately the full suppression of the Kapitza instability.  
49 This linear stabilization due to confinement was confirmed experimentally in Lavalle  
50 *et al.* (2019) for a water film in contact with quiescent air in a slightly inclined channel  
51 ( $\beta = 1.69^\circ$ ) of height  $H = 5$  mm. The main ingredient involved in the stabilization  
52 mechanism was found to be the tangential viscous stress exerted by the gas on the film  
53 surface, as suggested by Tilley *et al.* (1994). The strong stabilizing effect induced by a  
54 counter-current air flow on a wavy water film is reproduced by Trifonov (2019) at small  
55 inclination and strong confinement. Kushnir *et al.* (2021), via a comprehensive parametric  
56 study, have recently established that regimes of linear stabilization in the case of a zero  
57 net gas flow occur for channel heights  $H \leq 10$  mm at  $\beta = 1^\circ$  and  $H \leq 2$  mm at  $\beta = 10^\circ$   
58 in water/air system.

59 Furthermore, when the gas flows counter-currently, it was shown in Lavalle *et al.* (2019)  
60 that the linear stabilization is intensified over the entire range of unstable wave numbers  
61 when the confinement is sufficiently strong. For intermediate confinement levels, the  
62 linear effect of the gas flow can become non-monotonic, i.e. the cut-off wave number of  
63 the Kapitza instability first decreases and then increases with the gas flow rate (Vellingiri  
64 *et al.* 2015; Trifonov 2017; Lavalle *et al.* 2019). The stabilizing effect observed at low gas  
65 flow rate arises at all wave numbers. By contrast, when the gas flow rate is large, short  
66 waves are attenuated while long waves are amplified, in accordance with the experiments  
67 of Alekseenko *et al.* (2009) and Vellingiri *et al.* (2015) on linear waves in a vertically-falling  
68 liquid film, which were conducted in a vertical tube with a turbulent counter-current gas  
69 flow. Finally, for weak confinement, a monotonic increase of the cut-off wave number is  
70 observed and the destabilization of the film arises at all wave numbers.

71 The nonlinear response of surface waves has also been studied in a number of works,  
72 usually involving a turbulent counter-current gas flow in the context of flooding (Trifonov  
73 2010; Tseluiko & Kalliadasis 2011; Drosos *et al.* 2006; Vlachos *et al.* 2001; Kofman *et al.*  
74 2017). These studies, which concerned weak confinement levels or vertical configurations  
75 revealed that the amplitude of nonlinear waves increases and steepens with increasing  
76 gas flow rate while their speed decreases. The authors also observed that capillary ripples  
77 in front of the solitary waves are damped, in line with the linear stabilization of short  
78 waves observed by Alekseenko *et al.* (2009). In the weakly-confined setting, flooding  
79 manifests itself in experiments as wave reversal or wave breaking phenomena (Kofman  
80 *et al.* 2017; Drosos *et al.* 2006) emerging from the interfacial shear stress imposed by the  
81 gas flow. By contrast, in strongly-confined vertical channels, flooding is usually associated  
82 with a wave-induced local obstruction of the channel cross section (Vlachos *et al.* 2001;  
83 Dietze & Ruyer-Quil 2013), which can coincide with wave reversal events (Lavalle *et al.*  
84 2020). In such configurations, the counter-current gas flow amplifies the wave height and  
85 thus increases the flooding risk. Recent numerical investigations suggest that this trend  
86 could be inverted in weakly-inclined channels. For example, Trifonov (2019) identified  
87 a non-monotonic variation of the interfacial velocity, mean film thickness and inter-  
88 phase friction coefficient with increasing counter-current gas velocity, although the trend  
89 of the wave amplitude remained monotonic and increasing. Lavalle *et al.* (2021) have  
90 identified regimes where the nonlinear wave height and the linear growth rate both

91 decrease with increasing gas flow rate. Such regimes, if confirmed experimentally, could  
 92 avoid catastrophic flooding events, while exploiting the benefits of surface waves (e.g.  
 93 intensification of heat and mass transfer).

94 The main aim of the current manuscript is to confirm the existence of such regimes  
 95 through experiments. We study the effect of a counter-current laminar air flow on forced  
 96 two-dimensional solitary waves resulting from the Kapitza instability in a weakly-inclined  
 97 ( $\beta = 4.9^\circ$ ) strongly-confined channel of 5 mm height. A particular attention has been paid  
 98 to the boundary conditions, specifically designed to avoid flooding due to outlet effects  
 99 at the end of the test section, thus allowing to focus on the wave dynamics in the core of  
 100 the channel. Temporal forcing is applied at the liquid inlet to force surface waves within  
 101 a buffer zone before they come into contact with the air flow. The influence of the gas  
 102 shear stress on the shape, amplitude and velocity of these nonlinear waves is investigated  
 103 and contrasted with the experiments of Kofman *et al.* (2017), which were performed in a  
 104 weakly-confined channel ( $H = 19$  mm) where the gas flow was turbulent. Furthermore,  
 105 we are interested in the effect of the surface waves on the mean film thickness when the  
 106 gas velocity is increased.

107 The paper is organised as follows. The experimental set-up and the measuring tech-  
 108 niques are presented in § 2. Results are presented in § 3, where we discuss the response of  
 109 nonlinear surface waves to an increase in counter-current gas flow rate. In § 3.1, we focus  
 110 on the role of the confinement level, by contrasting our results with the weakly-confined  
 111 experiments of Kofman *et al.* (2017). **In § 3.2, we focus on the effect of the counter-current**  
 112 **gas flow on the dynamics of precursory capillary ripples. In § 3.3, we discuss the role of**  
 113 **the liquid Reynolds number and finally in § 3.4 we assess the effect of surface waves on**  
 114 **the mean film thickness.** Conclusions are drawn in § 4.

## 115 2. Experimental set-up and measurement methods

116 A general view of the experimental apparatus is sketched in figure 1: a liquid film falling  
 117 on the bottom plate of an inclined rectangular channel in contact with a counter-current  
 118 gas flow. Figure 2 displays a cross-sectional view of the channel. The liquid-related part  
 119 is the same as the one used in Lavallo *et al.* (2019). In subsection 2.1, we recall briefly  
 120 its main characteristics. Then in subsection 2.2 we describe the part related to the gas  
 121 phase.

### 122 2.1. Liquid loop

123 The liquid-related part consists in an inclined glass plate ( $L = 150$  cm long,  $W = 27$  cm  
 124 wide and 5 mm thick) placed on a massive framework mounted on rubber feet to dampen  
 125 environmental vibrations. The inclination angle  $\beta$  can be changed in the range  $0^\circ - 20^\circ$   
 126 and is measured using an inclinometer with a precision of  $0.05^\circ$ . In this work  $\beta$  is fixed to  
 127  $4.9^\circ$ . At the channel exit, the glass plate is extended with a porous medium that drains  
 128 the liquid away, allowing to avoid flooding events due to exit effects. A gear pump brings  
 129 the liquid from the outlet tank located at the exit of the plane to an inlet tank, from  
 130 which the liquid overflows and runs onto the plane. The volumetric liquid flow rate,  $q_l$ , is  
 131 changed by varying the pump power and is measured by using a magnetic-induced flow  
 132 meter. The liquid Reynolds number is calculated as:

$$133 \quad Re_l = \frac{q_l}{\nu_l W}, \quad (2.1)$$

133 where  $\nu_l$  is the kinematic viscosity of the liquid.

134 In this study,  $Re_l$  is varied in the range 20 - 49. A temporal periodic forcing of the

4

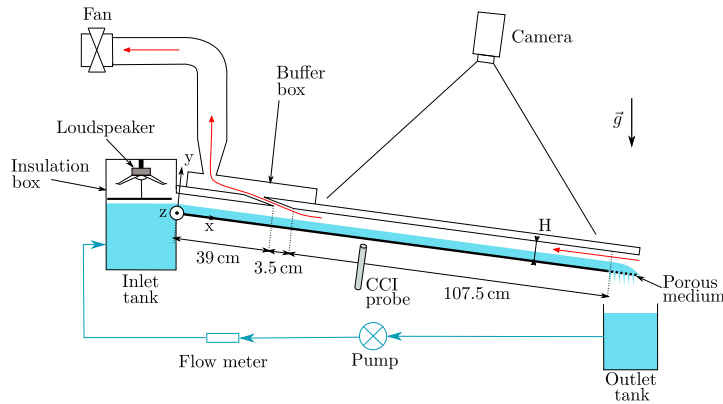


Figure 1: Sketch of the experimental set-up. The liquid loop appears in blue and the gas path is highlighted by red arrow.

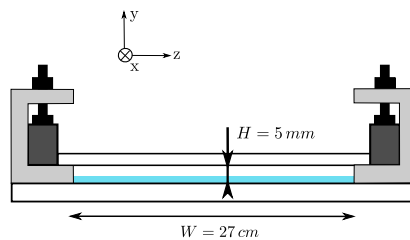


Figure 2: Sketch of the channel cross-section.

135 film is introduced at the inlet to trigger surface waves of prescribed frequency  $f$ . This  
 136 is achieved through a thin aluminium plate fixed to the membrane of two loudspeakers  
 137 thus generating harmonic vibrations above the liquid surface across the whole width of  
 138 the inlet tank (Kofman *et al.* 2017). **The choice of the forcing frequency depends on**  
 139  **$Re_l$  and is based on the aerostatic case (without counter-current gas flow). We adjust it**  
 140 **such that 2D saturated travelling waves are observed at the end of the unsheared zone**  
 141 **while avoiding secondary subharmonic or side-band instability (Liu & Gollub 1994). The**  
 142 **waves then form a regular wave train over the working area and appear as a large hump**  
 143 **preceded by capillary ripples.**

144 Water is used as working liquid. The temperature of the liquid is measured in the outlet  
 145 tank and upstream of the inlet tank. The surface tension is regularly monitored by taking  
 146 a water sample then using a drop shape analyser. A one-point temporal measurement of  
 147 the film thickness based on the CCI (Confocal Chromatic Imaging) technique (Cohen-  
 148 Sabban *et al.* 2001) is performed through the bottom glass plate with a spatial precision  
 149 of 250 nm and a temporal resolution up to 2 kHz. The CCI probe is mounted on a linear  
 150 translation stage in order to perform measurements along the streamwise axis of the  
 151 glass plate. In this study, the film thickness is measured at mid-width and at  $x = 60$  cm  
 152 from the inlet (see figure 1). An example of a CCI time trace is shown in figure 3a. From  
 153 such temporal measurements, we can extract: the time-averaged film thickness,  $h_m$  (blue  
 154 line) and the film thickness range, given by  $h_{max}$  and  $h_{min}$ , which correspond to the  
 155 statistical mean of the maximum and minimum wave height values measured over the  
 156 duration of the signal (red line and green line). **The temporal fluctuations of  $h_{max}$  and**  
 157  **$h_{min}$  are quantified from the standard deviation of the statistical measurements and are**

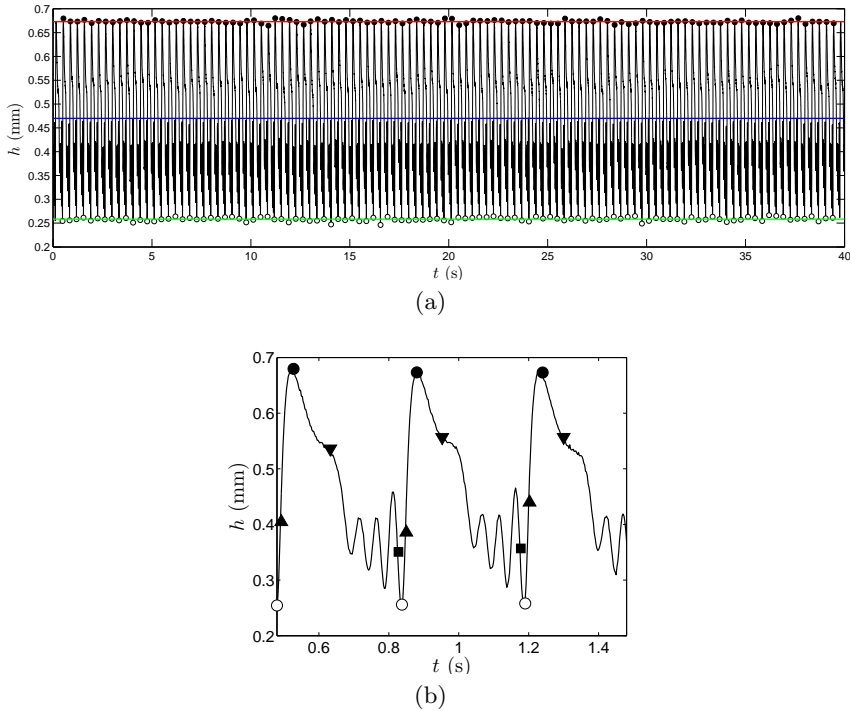


Figure 3: Film thickness time trace measured with the CCI technique.  $Re_l = 35$ ,  $f = 2.8$  Hz,  $\eta_0 = 11.1$ , without counter-current gas flow. (a) The blue line corresponds to the time-averaged film thickness over the duration of the signal. Open and filled circles correspond to the minimal and maximal height of each wave in the signal, respectively. (b) Enlargement of the signal presented in (a). Squares and downward triangles mark the maximum positive free-surface slope magnitude, located at the back of the first capillary wave and at the main wave tail. Upward triangles mark the maximum negative free-surface slope magnitude, located at the main wave front.

158 **used to include error bars in the relevant figures.** In addition, we can extract the local  
 159 free-surface temporal slope,  $\partial_t h$ , and calculate the statistical mean of its maximum and  
 160 minimum values over the duration of the signal, **as well as the related standard deviation.**  
 161 Figure 3b represents a blown up view over three wave periods, where we have highlighted  
 162 the maximum (positive) and minimum (negative) free-surface slope magnitude, located  
 163 at the back of the first capillary wave (**square**) and at the main front (**upward triangle**),  
 164 respectively. **The maximum free-surface slope magnitude is also indicated downward**  
 165 **triangle).**

166 For a given liquid Reynolds number, we quantify the relative confinement of the liquid  
 167 film with the global parameter:

$$\eta_0 = \frac{H}{h_m^0}, \quad (2.2)$$

168 where  $h_m^0$  is the time-averaged film thickness measured in the case of a quiescent gas  
 169 (superscript 0), i.e. without imposing a counter-current gas flow.

170 In addition to the pointwise CCI film thickness measurement, we visualize the film  
 171 surface with shadowgraphy. For this, the film is illuminated with an oblique white light

6

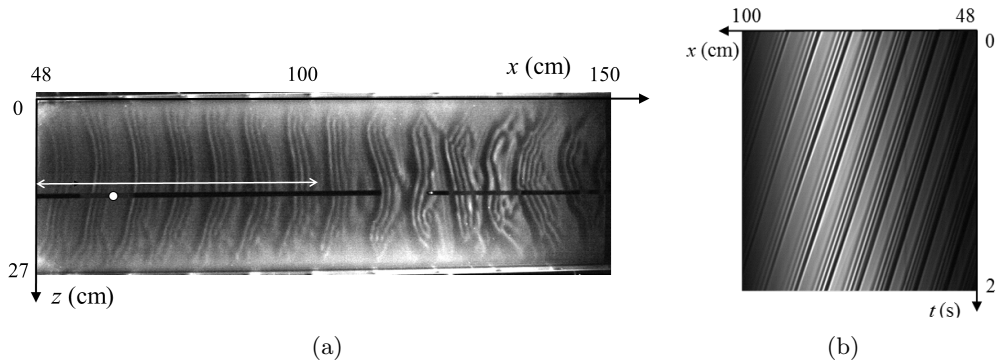


Figure 4: Typical experiment:  $Re_l = 35$ ,  $f = 2.8$  Hz,  $\eta_0 = 11.1$ , without counter-current gas flow (aerostatic case). (a) Visualisation of the gas/liquid interface over the entire test section. The white arrow marks the length over which spatiotemporal diagrams are constructed. The filled white circle marks the location for the CCI measurements ( $x = 60$  cm), (b) Spatiotemporal diagram obtained using a linear camera located in the midplane ( $z = 13.5$  cm).

172 sheet and imaged from the top either by a 2D camera to provide shadowgraphs over whole  
 173 width and length of the working area (figure 4a) or by a linear CCD camera focused on  
 174 the central axis ( $z = 0.5W$ ) to obtain spatio-temporal diagrams (figure 4b) from which  
 175 the wave speed,  $c$ , is determined. **At least two spatio-temporal diagrams are acquired for**  
 176 **each experiment and we measure the velocity of several waves around  $x = 60$  cm on each**  
 177 **diagram.  $c$  is then the mean of the set of measurements and the related error is given by**  
 178 **corresponding the standard deviation.** The wave speed can also be used to convert the  
 179 temporal slope  $\partial_t h$  of the film surface to the spatial slope  $\partial_x h = \partial_t h / c$ .

180

## 2.2. Gas loop

181 The gas flow is confined between the surface of the falling liquid film, which flows on  
 182 the bottom glass plate, and an upper 5 mm thick glass plate placed at a distance  $H$  from  
 183 the bottom one. The uniformity of  $H$  is regularly checked both in the streamwise and the  
 184 transverse direction, based on measurements with the CCI method. From one experiment  
 185 to another,  $H$  can vary from 5 mm to 5.2 mm depending on the force applied by the  
 186 screws to fix the top plate, but its variation for a given experiment is less than 0.5%.  
 187 Ambient air is sucked through the channel using a fan (see figure 1). The gas flow enters  
 188 the channel at the lower end and leaves through an outlet slot spanning the entire width  
 189 of the top plate. This slot ranges from  $x = 39$  cm to  $x = 42.5$  cm and opens into a buffer  
 190 box to which the fan is connected via a flexible pipe. Upstream of the slot ( $x < 39$  cm),  
 191 the liquid film is allowed to develop without being disturbed by the gas flow.

192 The air flow rate,  $q_g$ , is controlled by the fan power and is quantified based on a  
 193 calibration curve, which was obtained by measuring velocity profiles over the channel  
 194 height with a hot-wire anemometer, at different fan powers. The procedure is detailed  
 195 in the appendix A. These calibration measurements were performed in the absence of a  
 196 liquid film and we define a gas Reynolds number as:

$$Re_g = \frac{q_g}{\nu_g W}, \quad (2.3)$$



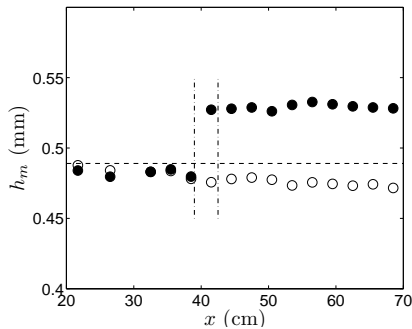


Figure 5: Streamwise evolution of the time-averaged film thickness,  $h_m$  along the central axis of the channel, in the aerostatic case ( $Re_g = 0$ , empty circles) and with counter-current gas flow ( $Re_g = 942$  ( $u_g = 3.05$  m/s), filled circles). The horizontal dashed-line indicates the Nusselt thickness (flat-surface film thickness without gas flow) associated to the prescribed liquid Reynolds number. The opening slot through which ambient air is sucked spans from  $x = 39$  cm to  $x = 42$  cm (highlighted by vertical dot-dash lines).  $Re_l = 35$ ,  $f = 2.8$  Hz,  $\eta_0 = 11$ .

197 where  $\nu_g$  is the kinematic viscosity of the gas and  $q_g$  is the gas flow rate measured in a  
 198 dry channel at the same fan power.

199 For the range of parameters used in this study, we assume that for a given fan power,  
 200 the air flow rate is not significantly affected by the presence of the liquid film in the  
 201 channel and thus the  $Re_g$  values are representative of the gas flow rate in the falling  
 202 liquid film experiments. This statement is discussed at the end of appendix A.

203 In this paper,  $Re_g$  was varied up to 1350, beyond which flooding occurs in the channel  
 204 for the liquid Reynolds number values considered. Experiments performed by Patel &  
 205 Head (1969) in a rectangular channel of aspect ratio  $W/H = 48$ , which is comparable to  
 206 the confined channel used in this paper ( $W/H = 54$ ), showed that the flow remains  
 207 laminar up to  $Re_g = 1300$  and becomes fully turbulent for  $Re_g > 2800$ . Velocity  
 208 measurements conducted in our channel and presented in appendix A confirmed that  
 209 the laminar-turbulent transition starts at  $Re_g > 1200$ . We can thus conclude that the  
 210 gas flow is laminar in the experiments presented in this paper.

211 The mean gas velocity,  $u_g$ , is defined as the spatially averaged velocity over the gas  
 212 cross-section and is determined from  $q_g$ :

$$u_g = \frac{q_g}{W(H - h_m)}, \quad (2.4)$$

213 where  $h_m$  is the time-averaged film thickness measured in the presence of the counter-  
 214 current gas flow.  $h_m$  remains almost constant along the central axis of the channel in  
 215 the sheared region (i.e. downstream of the slot) for a given gas flow rate, as shown in  
 216 figure 5 (filled circles). So we can consider that the mean gas velocity does not depend  
 217 on the streamwise position. Figure 5 also shows that the liquid film is not affected by  
 218 the counter-current gas flow in the unsheared zone upstream of the slot ( $x < 39$  cm).  
 219 Finally, this figure highlights the influence of the waves on the mean film thickness. We  
 220 observe that the measured mean film thickness without imposed counter-current gas flow  
 221 (empty circles) matches the primary-flow solution (dashed line) near the liquid inlet, then  
 222 it decreases in the streamwise direction as the surface waves develop due to secondary  
 223 instability.

8

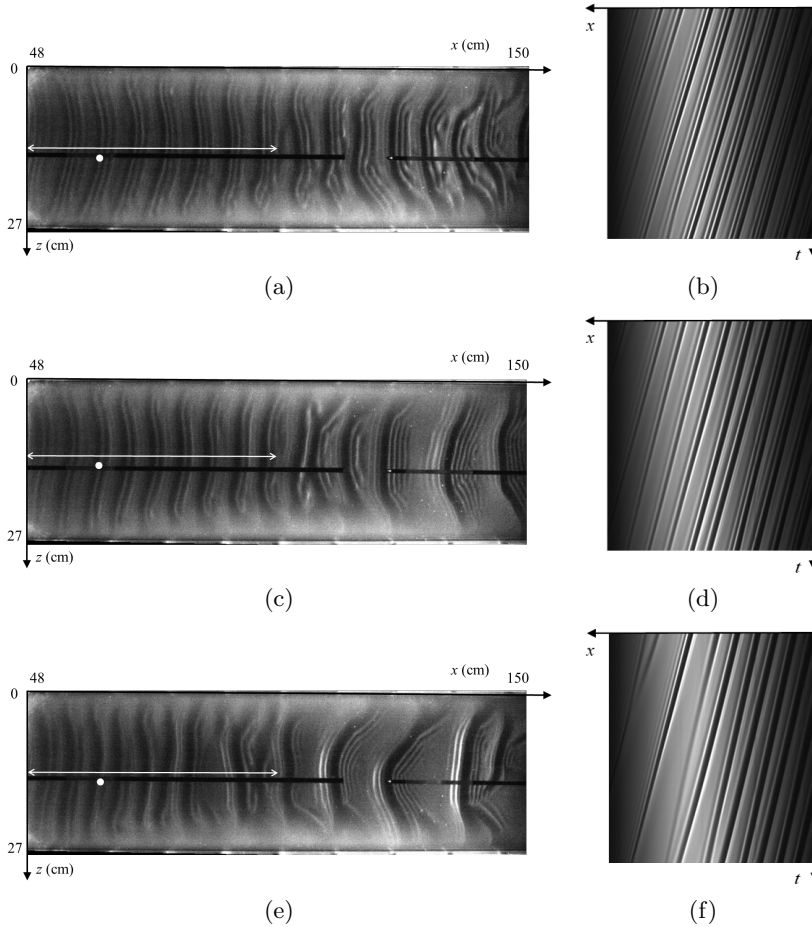


Figure 6: (a, c, e) Shadowgraphs of the gas/liquid interface over the entire test section for three different gas velocities, (b, d, f) associated spatio-temporal diagrams. From top to bottom:  $u_g = 1.9$  m/s ( $Re_g = 587$ ),  $u_g = 3.4$  m/s ( $Re_g = 1023$ ),  $u_g = 4.1$  m/s ( $Re_g = 1242$ ). These figures are the continuation of the aerostatic case ( $u_g = 0$ ) presented in figure 4. The white dot and arrow are the same as those described in the caption of figure 4.  $Re_l = 35$ ,  $f = 2.8$  Hz,  $\eta_0 = 11.1$ .

### 3. Results

Figure 6 displays shadowgraphs of the film surface and the corresponding spatio-temporal diagrams for different gas velocities at  $Re_l = 35$  and  $f = 2.8$  Hz. Increasing the gas velocity generates interactions between waves that can induce coalescence events, clearly visible in figure 6f, resulting in solitary waves of high amplitude preceded by numerous capillary ripples in the downstream portion of the plane (figures 6c and 6e). The initial regular wavetrain is progressively disrupted by the counter-current gas flow as one moves downstream, but it remains globally two-dimensional before merging occurs. In this study, we are interested in this region of 2D travelling waves, so measurements are performed at the location indicated by the white mark in figures 6a, 6c and 6e. In particular, we wish to know the nonlinear response of these waves to the strongly-confined counter-current gas flow.

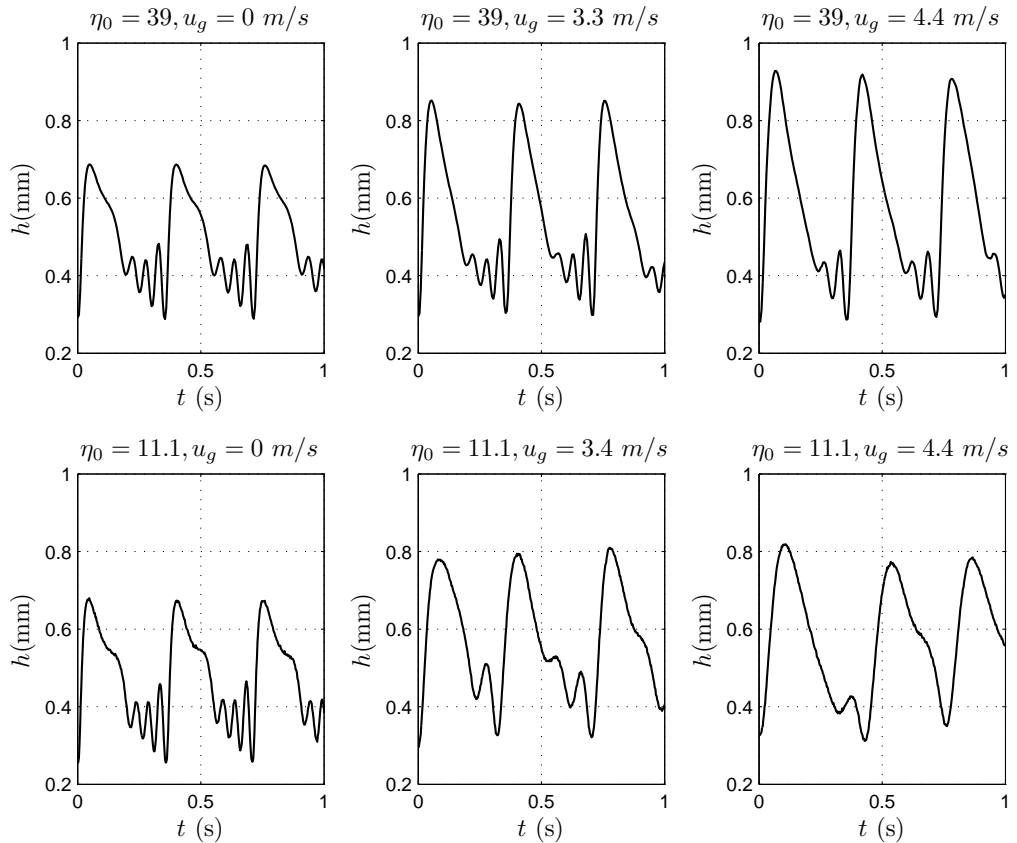


Figure 7: Influence of the gas velocity  $u_g$  on nonlinear wave profiles for two confinement levels:  $\eta_0 = 39$  ( $H = 19$  mm) and  $\eta_0 = 11.1$  ( $H = 5.2$  mm).  $Re_l = 35$ ,  $f = 2.8$  Hz,  $x = 60$  cm.

### 3.1. Effect of confined counter-current gas flow on 2D saturated travelling waves

In this section, we confront the results obtained in our strongly-confined channel with previous experiments conducted in a larger channel (Kofman *et al.* 2017). We consider a liquid film flowing at  $Re_l = 35$  on which we force travelling waves of frequency  $f = 2.8$  Hz through our coherent inlet forcing. We are interested in studying the effect of the counter-current gas flow on these waves, and, in particular, how this effect changes depending on the channel height.

Figure 7 confronts time records of the film thickness for the  $H = 19$  mm channel (top panels), which corresponds to a relative confinement  $\eta_0 = 39$  (Kofman *et al.* 2017), with those measured in our strongly-confined  $H = 5.2$  mm channel (bottom panels), where  $\eta_0 = 11.1$ . The measurement point was located at  $x = 60$  cm from the liquid inlet in both experiments. Without imposed gas flow ( $u_g = 0$ , left panels in figure 7) the wave train is identical in both cases, consisting in waves with a large-amplitude asymmetric hump preceded by three capillary ripples. Thus, the level of confinement is inconsequential for the aerostatic configuration. Starting from this reference state, we compare the response of solitary waves to a gradual increase of the gas velocity for both confinements (central and right panels in figure 7). The striking difference between the two cases is that the maximum film height gradually increases with  $u_g$  in the large channel whereas it levels off

10

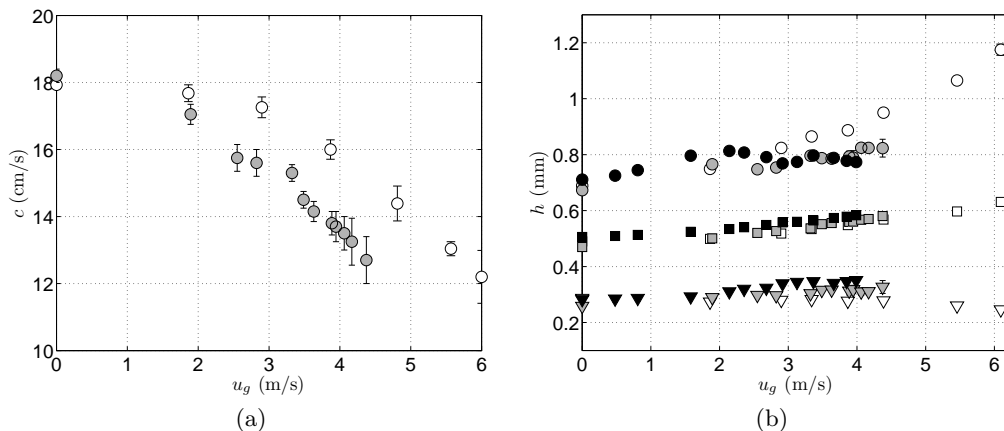


Figure 8: Influence of the gas velocity  $u_g$  on: (a) wave celerity  $c$ , (b) minimum  $h_{min}$  (downward triangles), mean  $h_m$  (squares) and maximum  $h_{max}$  (circles) film thickness for  $\eta_0 = 39$ ,  $\eta_0 = 11.1$  and  $\eta_0 = 9.9$  (white, grey and black symbols, respectively).  $Re_l = 35$ ,  $f = 2.8$  Hz,  $x = 60$  cm.

254 in the strongly-confined case. We also observe that the counter-current air flow attenuates  
 255 the capillary ripples ahead of the main hump, as discussed in (Kofman *et al.* 2017). This  
 256 effect is much more pronounced in the strongly-confined channel.

257 Figure 8 quantifies the gas effect on the wave characteristics for these two confinement  
 258 levels. Figure 8a displays the effect of the gas on the wave velocity,  $c$ , and figure 8b  
 259 its effect on the minimal ( $h_{min}$ ), averaged ( $h_m$ ) and maximal ( $h_{max}$ ) values of the film  
 260 thickness. We find that the slowing of the waves caused by the counter-current flow  
 261 is more pronounced in the strongly-confined channel than in the larger one. Figure 8b  
 262 shows that  $h_{min}$  and  $h_{max}$  are influenced by the confinement.  $h_{min}$  slightly increases  
 263 with  $u_g$  in the strongly-confined channel while it remains constant in the large channel,  
 264 or even slightly decreases for high gas velocities. As shown in figure 7,  $h_{max}$  in the  
 265 strongly-confined channel increases with  $u_g$  in a first stage ( $u_g < 2.1$  m/s for  $\eta_0 = 11.1$ )  
 266 then saturates, whereas it continuously increases in the large channel. By contrast,  $h_m$   
 267 increases by the same amount with  $u_g$  in all experiments, regardless of the confinement  
 268 level. In order to account for this increase in the mean film thickness, we report in figure  
 269 9 the normalized quantities:

$$\delta_{max} = \frac{h_{max}}{h_m} \quad (3.1)$$

270 based on the data from figure 8b.

271 For  $\eta_0 = 39$  ( $H = 19$  mm),  $\delta_{max}$  monotonously increases with  $u_g$  (open circles). Thus,  
 272 increasing the gas flow rate amplifies the nonlinear waves, which implies a destabilizing  
 273 (nonlinear) effect. This behaviour has been reported in several numerical studies (Tri-  
 274 fonov 2010, 2019; Tseluiko & Kalliadasis 2011). By contrast, for the strongly-confined  
 275 channel,  $\delta_{max}$  first increases but then clearly decreases with  $u_g$  (filled circles), in partic-  
 276 ular for  $\eta_0 = 9.9$ . These results confirm experimentally the numerical finding of Lavalle  
 277 *et al.* (2021) that increasing the counter-current gas flow can attenuate nonlinear waves.

278 For the strongly-confined channel, the attenuation of nonlinear waves observed in figure  
 279 9 sets in at  $u_g > 2$  m/s. As shown in figure 8a, this coincides with a sharp drop in  
 280 wave celerity under the effect of the gas which is much more pronounced in the strongly

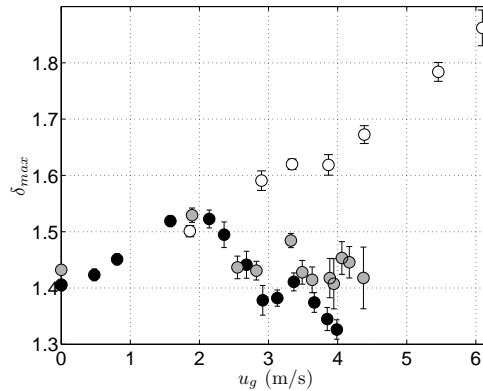


Figure 9: Influence of the gas velocity  $u_g$  on  $\delta_{max}$  (3.1) for  $\eta_0 = 39$ ,  $\eta_0 = 11.1$  and  $\eta_0 = 9.9$  (white, grey and black symbols, respectively).  $Re_l = 35$ ,  $f = 2.8$  Hz,  $x = 60$  cm.

281 confined channel than in the large channel. In figure 9, the wave amplitude curve  $\delta_{max}(u_g)$   
 282 exhibits a saw-tooth shape during the stabilizing stage ( $u_g > 2$  m/s) that will be discussed  
 283 in the next subsection. For  $\eta_0 = 11.1$  (grey symbols) the increase in  $\delta_{max}(u_g)$  which  
 284 reflects a re-destabilization of the waves between  $u_g = 2.9$  m/s and  $u_g = 3.3$  m/s is  
 285 correlated to the modulation in the wave celerity depicted in figure 8a (grey symbols)  
 286 which means that the stabilization mechanism is very sensitive to the wave celerity.

### 3.2. Effect of the counter-current gas flow on precursory capillary ripples

287  
 288 The saw-tooth shape exhibited in figure 9 for the strongly-confined channel at  $u_g >$   
 289  $2.1$  m/s is correlated to the wave celerity and results in a sequential suppression of  
 290 capillary ripples under the effect of an increasing gas flow, as shown in figure 10, where  
 291 wave profiles at different gas velocities are displayed for  $\eta_0 = 9.9$  (black symbols in  
 292 figure 9). For  $u_g < 2.1$  m/s the effect of the counter-current gas is to increase the wave  
 293 amplitude without significantly affecting the wave speed and the number of capillary  
 294 ripples remains unchanged (in this case, 3 capillary ripples are observed ahead of the main  
 295 hump). For  $u_g > 2.1$  m/s, the wave speed drops significantly, which reduces the  
 296 wavelength of the main waves ( $f = 2.8$  Hz is constant here). Both effects are known  
 297 to reduce the number and amplitude of precursory capillary ripples (Dietze 2016), and  
 298 this is observed in figure 10 ( $\eta_0 = 9.9$ ): we move from 3 to 2 capillary ripples between  
 299  $u_g = 2.9$  m/s (alternation of 2 or 3 capillary ripples) and  $u_g = 3.1$  m/s (2 capillary  
 300 ripples) and from 2 to 1 at  $u_g = 3.8$  m/s just before flooding. For  $\eta_0 = 11.1$  (grey  
 301 symbols in figure 9) the transition 3 – 2 and 2 – 1 occurs at  $u_g \simeq 2.6$  m/s and 3.6 m/s.  
 302 The change in the number of capillary ripples correspond to the troughs of the saw-tooth  
 303 shape in figure 9.

304 To confirm that the number of capillary ripples is indeed governed by the wave speed,  
 305 figures 11 compares the maximum positive slope,  $\max\{\partial_x h\}$ , for the two confinement  
 306 levels  $\eta_0 = 11.1$  (grey symbols) and  $\eta_0 = 39$  (white symbols). This maximum is observed  
 307 at the back of the first capillary ripple (squares in figure 3b) and is an indicator of the  
 308 compression of the capillary wave train due to the decrease of the wave length. Figure 11a  
 309 displays  $\max\{\partial_x h\}$  (square symbols) as a function of  $u_g$ , and Figure 11b as a function  
 310 of the normalized wave velocity  $\hat{c}$ :

12

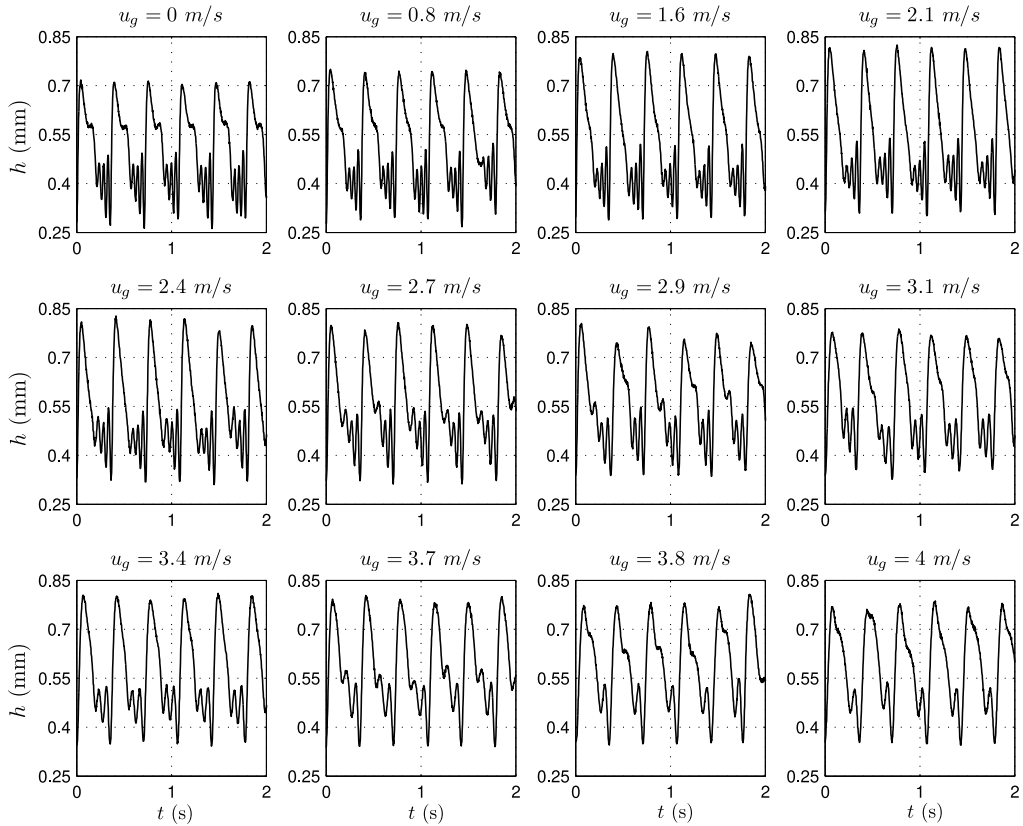


Figure 10: Influence of the gas velocity  $u_g$  on nonlinear wave profiles measured at  $x = 60$  cm for  $Re_l = 35$ ,  $f = 2.8$  Hz,  $\eta_0 = 9.9$ , corresponding to the experiment presented in figure 9 (black symbols).

$$\hat{c} = \frac{c_0 - c}{c_N}, \quad (3.2)$$

311 where  $c_N = \frac{gh_N^2 \sin \beta}{\nu_l}$  is the speed of kinematic waves in a passive atmosphere,  $c_0$   
 312 corresponds to the measured wave speed in the case of a quiescent gas, and  $h_N =$   
 313  $\left(\frac{3q_l \nu_l}{\sin \beta g}\right)^{1/3}$  is the Nusselt thickness (the flat-surface film thickness in the passive-gas  
 314 limit).

315 Figure 11a shows that for a given value of  $u_g \neq 0$ , the slope magnitude at the back  
 316 of the first capillary ripple as well as the number of capillary ripples depend on the  
 317 confinement. By contrast, figure 11b shows that for a given value of  $\hat{c}$  these quantities  
 318 are identical regardless of the confinement, which is also clearly visible from wave profiles  
 319 presented in figure 12 for  $\hat{c} = 0.13$  and  $\hat{c} = 0.23$  (marked by vertical dashed lines in  
 320 figure 11b). This behaviour implies that the capillary region is not directly affected by  
 321 the gas shear-stress but is controlled by the indirect effect of the gas-induced slowing  
 322 of the large waves. In figure 11 we have also plotted the maximum negative slope  $\min \{\partial_x h\}$   
 323 at the main hump front (upward triangles) which is an indicator of the steepness of the  
 324 wave, and the maximum (positive) slope at the wave tail (downward triangles). In the

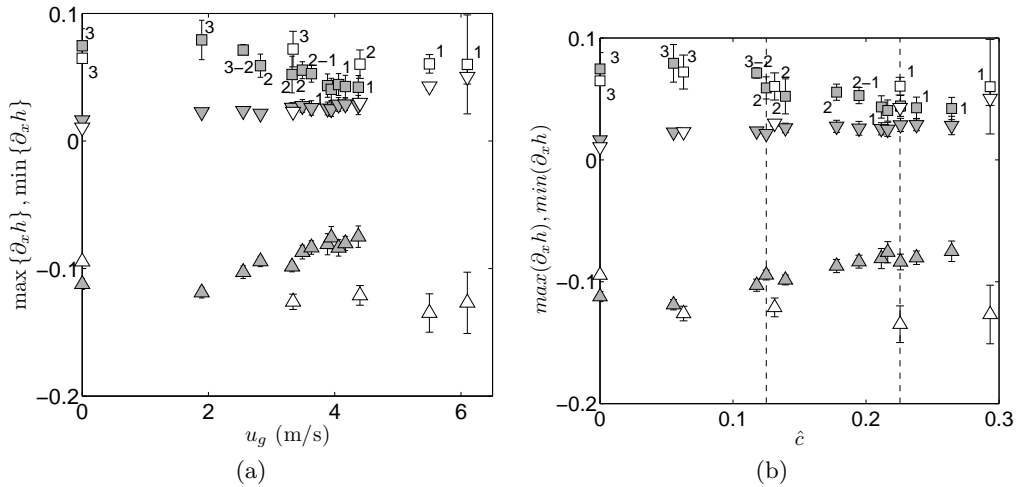


Figure 11: Influence of the gas velocity  $u_g$  in (a) and the normalized gas velocity  $\hat{c}$  (3.2) in (b), on the maximum positive free-surface slope  $\max\{\partial_x h\}$  at the back of the first capillary ripple (squares) and at the main hump tail (downward triangles), and on the maximum negative slope  $\min\{\partial_x h\}$  at the front of the main hump (upward triangles), for  $\eta_0 = 39$  (white symbols) and  $\eta_0 = 11.1$  (grey symbols). The number of capillary ripples is indicated. Vertical dashed lines in (b) indicate the values of  $\hat{c}$  related to the wave profiles presented in figure 12.  $f = 2.8$  Hz,  $Re_l = 35$ ,  $x = 60$  cm.

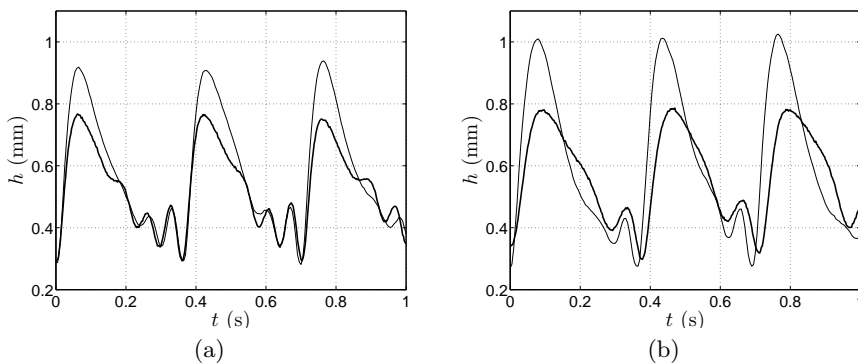


Figure 12: Influence of the confinement on wave profiles at given values of  $\hat{c}$  (3.2) marked by vertical dashed lines in figure 11b. (a)  $\hat{c} = 0.13$ , (b)  $\hat{c} = 0.23$ . Thin solid line:  $\eta_0 = 39$  ( $u_g = 4.4$  m/s in (a) and 5.5 m/s in (b)), thick solid line:  $\eta_0 = 11.1$  ( $u_g = 2.8$  m/s in (a) and 4 m/s in (b)). Same parameters as in figure 11.

325 large channel (white symbols) the front inclination remains unchanged as the gas velocity  
 326 is increased, while the tail steepens, thus resulting in a more symmetrical wave (thin solid  
 327 curves in figure 12). By contrast in the strongly-confined channel (grey symbols), the  
 328 front inclination weakens while the tail slope remains unchanged under the action of the  
 329 counter-current flow, and the resulting wave is less symmetrical than in the large channel  
 330 (thick solid curves in figure 12).

14

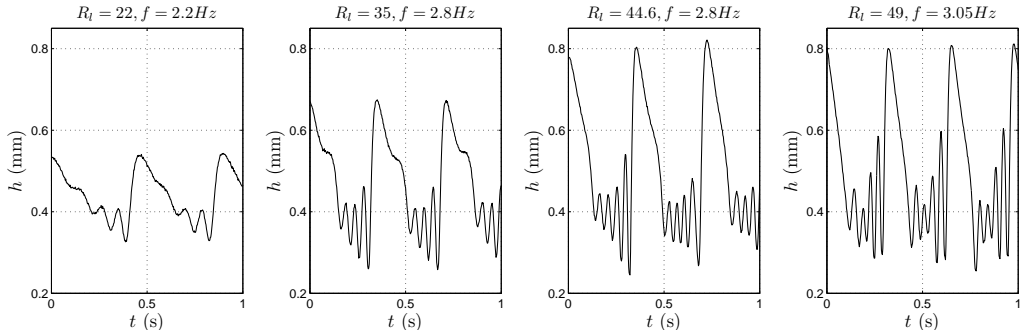


Figure 13: Wave profiles for different values of the liquid Reynolds number  $Re_l$  and forcing frequency  $f$  in the strongly-confined channel for the aerostatic case. From left to right, the resulting wavelength is 6.5 cm ( $Re_l = 22$ ), 6.5 cm ( $Re_l = 35$ ), 7.3 cm ( $Re_l = 44.6$ ), not available for  $Re_l = 49$ .

331

### 3.3. Influence of the liquid Reynolds number

332

333

334

335

336

337

338

339

340

341

We now investigate the effect of the counter-current gas flow on the response of nonlinear waves for different values of the liquid Reynolds number  $Re_l$  and the forcing frequency  $f$ , in the strongly-confined channel. As shown in figure 13 for the quiescent-gas reference case, these parameters clearly affect the mean film thickness and consequently the confinement level  $\eta_0$  (2.2), the maximum film thickness  $h_{max}$ , and the number of precursory capillary ripples. The forcing frequency has been empirically adjusted from the aerostatic case according to the liquid Reynolds number, in order to generate 2D saturated quasi-solitary waves in the working zone. The resulting wavelength of the unshered wave train is specified in the caption of figure 13 provided that wave velocity measurements are available.

342

343

344

345

346

347

348

349

350

351

352

353

354

355

We report in figure 14 the variation of  $c$  (figure 14a) and  $\delta_{max}$  (figure 14b) in terms of  $Re_g$  for different  $Re_l$  and forcing frequency  $f$ . For  $Re_l = 44.6$  (grey triangles), we observe the same overall behaviour as for  $Re_l = 35$ , which was presented in the previous section. In a first stage,  $\delta_{max}$  increases with  $Re_g$  (the gas flow is nonlinearly destabilizing) then decreases when  $c$  is significantly reduced (the gas flow is nonlinearly stabilizing), with saw-tooth modulations associated with the change in the number of capillary ripples, whereas the variation of  $c$  with  $Re_g$  remains monotonous. For a higher liquid flow rate,  $Re_l = 49$  (crosses), the destabilizing stage at low gas velocity is replaced by a stabilizing one. For the lowest Reynolds number,  $Re_l = 22$  (open triangles), there are only two capillary waves to start with (see first panel in figure 13) and we observe a weak stabilization until  $Re_g \approx 600$ , associated with the suppression of one capillary wave.  $\delta_{max}$  then increases to reach a constant value while maintaining one capillary wave until the experiment breaks down due to flooding downstream.

We now introduce the local relative confinement parameter  $\eta_{max}$  as:

$$\eta_{max} = \frac{H}{h_{max}} \quad (3.3)$$

356

357

358

Figure 15 displays  $\eta_{max}$  as a function of  $Re_g$  for the same parameters as figure 14. The gas-induced stabilization at  $Re_l = 22$  is associated with a relative confinement  $\eta_{max} \approx 9$ . For  $Re_l = 35, 45$  and  $49$  the stabilizing effect occurs for smaller confinement levels.



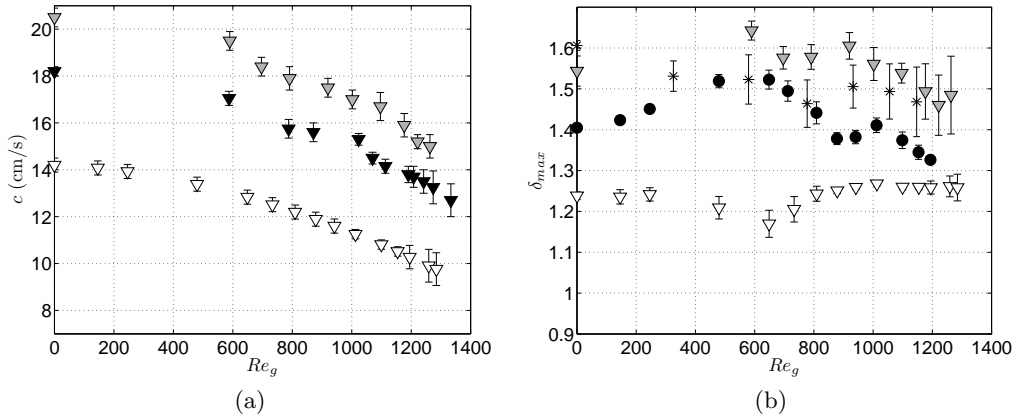


Figure 14: Influence of the liquid Reynolds number  $Re_l$  on: (a) wave celerity:  $Re_l = 22$ ,  $\eta_0 = 11.5$  (white triangles) -  $Re_l = 35$ ,  $\eta_0 = 11.1$  (black triangles) -  $Re_l = 44.6$ ,  $\eta_0 = 10.3$  (grey triangles), (b)  $\delta_{max} = h_{max}/h_m$ : same parameters as (a) for white and grey triangles,  $Re_l = 35$ ,  $\eta_0 = 9.9$  (black circles) -  $Re_l = 49$ ,  $\eta_0 = 10.3$  (crosses). Strongly-confined channel.

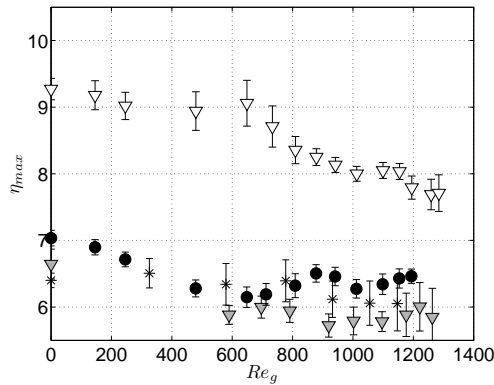


Figure 15: Influence of the liquid Reynolds number  $Re_l$  on the local confinement parameter  $\eta_{max}$  (3.3) in the strongly-confined channel. Same parameters as in figure 14b.

### 3.4. Effect of the surface waves on the mean film thickness

359

360 We now wish to gauge the effect of the gas-sheared surface waves on the mean film  
 361 thickness  $h_m$ . In particular, we wish to know whether  $h_m$  is decreased or increased  
 362 versus the primary-flow thickness. In the case of a passive gas or a quiescent unconfined  
 363 atmosphere, it is well known that  $h_m$  is smaller than the primary-flow thickness. This  
 364 is known as wave-induced effective film thinning (Miyara 1999). In our current case of a  
 365 counter-current gas flow, it turns out that the wave effect depends on the confinement  
 366 level. To group our measurement data for the  $H=5$  mm channel, where the gas flow is  
 367 laminar, and the data of Kofman *et al.* (2017) for an  $H=19$ mm channel, where the gas  
 368 flow is turbulent, we introduce the Froude number  $Fr_{g,l}$ , which relates interfacial shear  
 369 stress ( $\sim \rho_g u_g^2$ ) to gravitational effects:

16

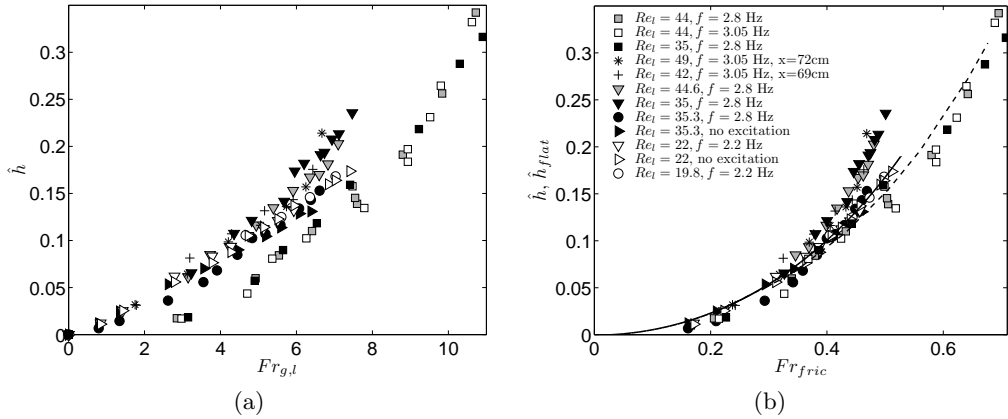


Figure 16: Relative mean film thickness  $\hat{h}$  (3.5) measured in the  $H \approx 5$  mm channel and in the  $H \approx 19$  mm channel (Kofman *et al.* (2017), square symbols), as a function of: (a) the Froude number  $Fr_{g,l}$  (3.4), (b) the modified Froude number,  $Fr_{fric}$  (3.6). The solid and dashed curves correspond to the flat-film solution  $\hat{h}_{flat}$  according to B13 with  $\epsilon = 0$  ( $\hat{h}_{flat} = \tilde{h}_{flat} - 1$ ).

$$Fr_{g,l} = \sqrt{\frac{\rho_g u_g^2}{\rho_l g \sin \beta h_N}}, \quad (3.4)$$

370 and the normalized film thickness  $\hat{h}$ :

$$\hat{h} = \frac{h_m}{h_m^0} - 1 \quad (3.5)$$

371 Figure 16a displays  $\hat{h}$  as a function of  $Fr_{g,l}$ , for all experiments conducted in the  
 372  $H = 5$  mm channel (different  $Re_l$  and  $f$ ), as well as the experiments of Kofman *et al.*  
 373 (2017) conducted in a  $H = 19$  mm channel (square symbols). The experimental data  
 374 collapse onto two different trends, one for the narrow channel and another for the wide  
 375 channel. This is due to the different flow regimes in the two configurations, the gas flow  
 376 being laminar in the former case and turbulent in the latter.

377 To account for this, we improve our approximation of the interfacial shear stress used  
 378 in (3.4) in a modified gas-liquid Froude number,  $Fr_{fric}$ , based on the friction velocity,  
 379  $u_{fric}$ :

$$Fr_{fric} = \sqrt{\frac{\rho_g u_{fric}^2}{\rho_l g \sin \beta h_N}} = \sqrt{\frac{C_{f,i}}{2}} Fr_{g,l}, \quad (3.6)$$

380 where  $u_{fric}$  is based on the tangential interfacial gas shear stress of the primary flow (no  
 381 waves),  $\tau_i$ , as:

$$u_{fric} = \sqrt{\frac{\tau_i}{\rho_g}} \quad (3.7)$$

382  $\tau_i$  is related to the global skin-friction coefficient,  $C_{f,i}$ :

$$C_{f,i} = \frac{\tau_i}{1/2 \rho_g u_g^2} \quad (3.8)$$

383 In the strongly-confined channel, the gas flow is laminar and we approximate  $C_{f,i}$  by  
 384 the relation for Poiseuille flow through a plane dry channel:

$$C_{f,i} = 12Re_g^{-1} \quad (3.9)$$

385 In the large channel the gas flow is fully turbulent and we use an experimental  
 386 correlation established by Patel & Head (1969) in a wide rectangular horizontal dry  
 387 channel:

$$C_{f,i} = 0.0376Re_g^{-1/6} \quad (3.10)$$

388 Using these correlations for  $C_{f,i}$ , we assume that the liquid-gas interface can be con-  
 389 sidered as immobile. To validate this motionless interface assumption, we have compared  
 390 the film thickness of a flat-surface film subject to a counter-current laminar gas flow as  
 391 obtained by numerical solution of the fully-coupled two-phase primary flow (Lavalle *et al.*  
 392 2019) with the thickness obtained by assuming an inter-phase skin friction coefficient  
 393 according to (3.9). Details on this flat-film model are given in appendix B. The two  
 394 predictions are in excellent agreement and this holds over the entire range of experimental  
 395 conditions studied in this work (see figure 23 in appendix B).

396 In figure 16b,  $\hat{h}$  (3.5) is plotted as a function of  $Fr_{fric}$ , according to (3.6). We observe  
 397 that the new scaling is more appropriate to describe the effect of the shear stress exerted  
 398 by the gas on the interface, as the laminar and turbulent data are now gathered. The  
 399 two additional solid and dashed curves correspond to the flat-film model  $\hat{h}_{flat}$  (according  
 400 to B 13 with  $\epsilon = 0$ ,  $\hat{h}_{flat} = \tilde{h}_{flat} - 1$ ) for the laminar gas flow in the strongly-confined  
 401 channel (solid line) and for the turbulent gas flow in the large channel (dashed line). **This**  
 402 **model represents a reference solution for comparison with the wavy experimental data.**

403 **The mean film thickness results from two opposing intricate effects: the well known**  
 404 **effective thinning due to nonlinear surface waves, illustrated in figure 5 for the aerostatic**  
 405 **case, and the thickening effect of the counter-current gas flow produced by the interfacial**  
 406 **shear-stress. The relative competition of these two effects determines the mean film**  
 407 **thickness ultimate behaviour.**

408 In the large channel (square symbols) the experimental data lie slightly below the flat-  
 409 film prediction. Thus, surface waves tend to reduce the mean film thickness, as in the  
 410 case of a quiescent atmosphere.

411 In the strongly-confined channel, at high liquid Reynolds number values  $Re_l$  and  
 412 high Froude numbers ( $Fr_{fric} \geq 0.35$ ), experimental data are clearly above the flat-  
 413 film prediction which means that the mean wavy film thickness grows faster than the  
 414 reference flat-film thickness. This behaviour occurs in the nonlinear stabilizing regime for  
 415 strong relative confinement levels, where surface waves promote a significant variation of  
 416 the gas cross-section, which in turn affects the local tangential shear stress. This is the  
 417 basis for the linear stabilization mechanism described by Lavalle *et al.* (2019). In this  
 418 regime, the gas effect tends to reduce the nonlinear amplitude of the main hump and thus  
 419 the thinning effect of the waves, while it increases the residual flat film thickness between  
 420 two humps. In figure 14b, we observe that during this stage, the interaction between the  
 421 liquid film and the counter-current gas flow generates strong disturbances of the wave  
 422 train as highlighted by the large temporal fluctuations measurements for  $Re_l = 44.6$  and  
 423 49.

424 By contrast, when  $Re_l$  and thus the wave amplitude is small, experimental data are well  
 425 predicted by the flat-film model over the entire range of the Froude number. In this case,  
 426 the mean thickness of the wavy film increases at the same rate as the flat film thickness  
 427 when the gas flow rate is increased, indicating that the thinning effect of the surface  
 428 waves balances the overall thickening effect due to the gas shear stress. **This balance**

429 can also be observed at higher  $Re_l$  and moderate Froude number values ( $Fr_{fric} \leq 0.35$ ,  
 430 crosses) for experiments concerned with the monotonously nonlinear stabilizing regime  
 431 (see crosses in figure 14b).

432 Further, we conclude that the interfacial shear stress effect on the nonlinear surface  
 433 waves changes by increasing the gas velocity in the strongly confined channel. This  
 434 behaviour could be related to the observations of Trifonov (2019), who performed simu-  
 435 lations of nonlinear waves for a set of parameters similar to our experimental conditions  
 436 ( $\beta = 5^\circ$ ,  $H = 5$  mm,  $Re_l = 5, 15$  and  $40$ , see the supplementary material associated with  
 437 the cited article). The author demonstrates the existence of a local minimum of the mean  
 438 film thickness and of the gas friction coefficient in terms of the gas superficial velocity.  
 439 More specifically, at  $Re_l = 40$ , he found that the decrease of the friction coefficient  
 440 deviates from the decreasing trend of the waveless solution ( $\propto 1/Re_g$ ) at a gas velocity  
 441 comparable to the experimental values associated to the deviation of  $h_m$  from the flat-film  
 442 solution observed in figure 16b.

443 The experimental data corresponding to the black filled circles deviates from the other  
 444 data at similar liquid Reynolds numbers. For this experiment the Kapitza number is  
 445 lower (by 13% due to a different ambient temperature) and the channel height  $H$  is  
 446 slightly lower (by 4%). These variations do not significantly affect the primary flow,  
 447 as can be inferred from the right-pointing triangles which correspond to an experiment  
 448 performed the same day without inlet forcing, and which lie on the solid curve related to  
 449 the primary flow solution. However, the destabilizing effect of the gas on the nonlinear  
 450 waves at moderate Froude number values may be enhanced, which could favor the wave-  
 451 induced effective film thinning effect (these data lie below the solid curve).

## 452 4. Conclusion

453 In this paper, experiments were conducted on water films falling along the bottom wall  
 454 of a weakly-inclined ( $\beta = 4.9^\circ$ ) rectangular channel of height  $H \approx 5$  mm interacting with  
 455 a laminar counter-current air flow. Surface waves were excited via coherent inlet forcing  
 456 before they come into contact with the air flow to promote travelling waves consisting in  
 457 a large-amplitude hump preceded by capillary ripples. We focused on the sheared region  
 458 of the film where the waves were two-dimensional without interaction between them.  
 459 Local film thickness time traces and wave celerity measurements have been performed  
 460 together with visual observations.

461 The effect of the air flow on the height, shape, and speed of the waves was investigated  
 462 and contrasted with results obtained by Kofman *et al.* (2017) in a channel of height  
 463 19 mm, where the counter-current gas flow was turbulent. The stronger confinement  
 464 level studied here versus the experiments of Kofman *et al.* (2017) not only changes the  
 465 geometrical constriction of the gas flow but also leads to a laminar flow regime in the  
 466 gas instead of a turbulent one. In experiments, these two effects, which play their own  
 467 distinct roles, cannot be decoupled. However, Trifonov (2010) has shown via numerical  
 468 simulations that the main effect of turbulence is to shift the onset of wave-induced critical  
 469 events (e.g. the flooding onset) toward lower superficial gas velocities.

470 In our experiments, no confinement-induced effect was detected on the wave dynamics  
 471 in the case of a quiescent gas. Indeed, the shape, amplitude and velocity of the nonlinear  
 472 waves excited at a prescribed frequency are almost identical for the two confinement  
 473 levels. When a counter-current gas flow is imposed, striking differences are observed.  
 474 For all the experiments conducted in the weakly confined channel, the effect of the gas  
 475 on the travelling nonlinear waves was destabilizing (see Kofman *et al.* (2017)), whereas

476 a monotonic stabilizing effect or a non-monotonic trend was observed in the strongly-  
477 confined channel, depending on the liquid Reynolds number  $Re_l$ .

478 For small  $Re_l$  in the strongly confined channel, inertia is weak and the relative  
479 confinement is quite low without gas flow ( $\eta_{max} > 9$ ). Under these conditions, the wave  
480 amplitude first slightly diminishes as the gas velocity is increased and then increases to  
481 reach a plateau sustaining one capillary ripple until onset of flooding. In that case, the  
482 stabilizing mechanism induced by the variation of the gas shear stress at the interface is  
483 quite weak.

484 For moderate  $Re_l$ , the wave amplitude first increases with the gas velocity while  
485 the number of capillary ripples ahead of the main hump and the wave celerity remain  
486 unchanged. Upon increasing the gas velocity further, the wave amplitude diminishes and  
487 a gradual reduction of the number of capillary ripples is observed. For higher values of  
488  $Re_l$ , a monotonically gas-induced wave attenuation is observed.

489 These experimental observations are in line with recent numerical results obtained by  
490 Lavalley *et al.* (2021) in a superconfined channel, where monotonic gas-induced amplifica-  
491 tion (attenuation) of the nonlinear wave amplitude was detected for larger (smaller)  $H$ ,  
492 and a non-monotonic trend was observed for intermediate  $H$ .

493 To quantify the effect of surface waves on the mean film thickness in a universal form,  
494 a modified Froude number has been constructed which relates viscous drag based on the  
495 skin friction coefficient and gravity. We have compared the normalized measured mean  
496 film thickness  $\hat{h}$  with the primary-flow solution  $\hat{h}_{flat}$  obtained in the limit of a frozen  
497 (immobile) liquid-gas interface. In the case of a turbulent gas flow, which corresponds to  
498 experiments conducted in the large channel,  $\hat{h}_{flat}$  is greater than  $\hat{h}$ . In these experiments,  
499 waves are significantly amplified by the counter-current flow and the wave-induced film  
500 thinning effect (Miyara 1999) is dominant compared to the thickening effect of the gas  
501 shear stress. In the laminar configuration, which corresponds to experiments conducted  
502 in the strongly confined channel,  $\hat{h}$  and  $\hat{h}_{flat}$  correspond when  $Re_l$  is small, which implies  
503 that the thinning effect of the waves on the mean thickness is balanced by the shear-  
504 stress thickening effect, and the experimental behaviour is well predicted by the model.  
505 For higher liquid Reynolds number values,  $\hat{h}_{flat} < \hat{h}$  in the range of parameters where  
506 the nonlinear stabilization occurs.

## 507 5. Acknowledgments

508 This work was supported by the ANR WavyFilm project, grant ANR-15-CE06-0016-01  
509 of the French Agence Nationale de la Recherche. The authors are grateful to Johannes  
510 Amrani, Alban Aubertin, Lionel Auffray and Rafaël Pidoux for their contribution to  
511 build the experimental set-up.

512 Declaration of Interests: the authors report no conflict of interest.

## 513 Appendix A. Measurement of the gas flow rate

514 In this section we describe the procedure that has been used to quantify the air flow rate  
515  $q_g$  generated by the fan in the inclined strongly-confined channel of figure 1. This quantity  
516 is used to evaluate the gas Reynolds number according to equation (2.3). This was done  
517 based on a calibration curve between a given fan power and the corresponding gas flow  
518 rate obtained from velocity measurements in the dry channel, i.e. without the liquid film.  
519 The porous medium at the end of the bottom glass plate was replaced by a Plexiglas  
520 plate with an opening to allow access for a hot-wire anemometer probe (see figure 17).  
521 With this probe, we measured the wall-normal profile of the streamwise velocity  $u(y)$

20

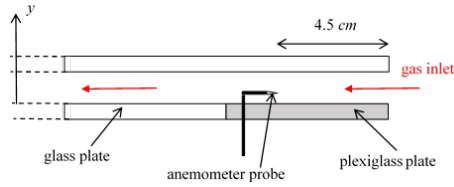


Figure 17: Location of the anemometer used to measure the air velocity at the end of the channel (gas inlet).

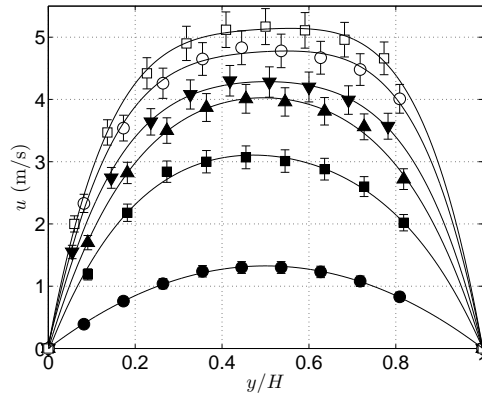


Figure 18: Air velocity profiles measured for different fan powers (in Watt) in the dry channel:  $P_f = 1.3$  (circles), 3.9 (squares), 6.5 (upward triangles), 7.8 (downward triangles), 10.4 (open circles) and 13 (open squares). Solid lines correspond to polynomial fits.  $\beta = 4.9^\circ$ .

522 at mid-width of the channel and 4.5 cm from the air inlet. Figure 18 displays profiles  
 523 obtained for different fan powers and for the inclination angle used in the experiments,  
 524  $\beta = 4.9^\circ$ . Each dot corresponds to a time-averaged measurement over 30 s and the error  
 525 bars are included according to the uncertainty of the probe given by the manufacturer.  
 526 A polynomial fit is performed for each profile from which we compute the air flow rate:

$$q_g = W \int_0^H u(y) dy, \quad (\text{A } 1)$$

527 where  $W = 27$  cm is the channel width. The calibration curve presented in figure 19  
 528 gives the air flow rate per unit width as a function of the imposed fan power,  $P_f$ . The  
 529 gas Reynolds number,  $Re_g$ , is then calculated using (2.3). When the fan is switched  
 530 off ( $P_f=0$ ), there is no gas flow in the dry channel, and, thus,  $Re_g=0$  according to our  
 531 procedure, even though a small non-zero gas flow would be generated in the presence of  
 532 a falling liquid film.

533 In figure 18, we have plotted several examples of measured velocity profiles for laminar  
 534 flow conditions (black symbols), i.e.  $Re_g < 1300$  according to the laminar-turbulent  
 535 transition threshold determined by Patel & Head (1969) in a high-aspect-ratio channel.  
 536 Table 1 reports the corresponding values of the velocity ratio  $u_g/u_{max}$ , where the  
 537 mean velocity  $u_g$  has been defined in (2.4) and  $u_{max}$  is the maximum velocity. The  
 538 aerodynamic entry length,  $L_d$ , is also reported, which is defined as the length needed for  
 539 the boundary layers along the two horizontal channel walls to join at  $y = H/2$ . Based

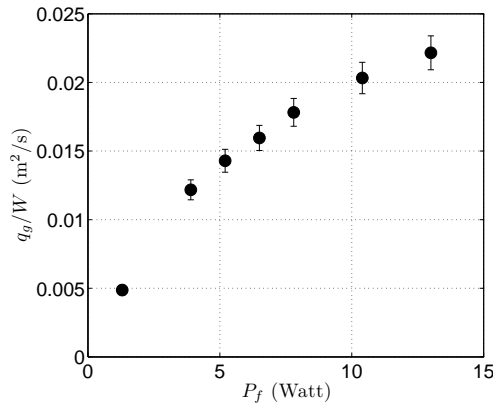


Figure 19: Calibration curve used to quantify the gas flow rate  $q_g$  (A 1) per unit of channel width from the imposed fan power  $P_f$ .  $\beta = 4.9^\circ$ .

Table 1: Ratio between the mean and the maximum air velocity issued from the measured velocity profiles (black symbols in figure 18) and the corresponding aerodynamic entry lengths given by (A 2).

| $Re_g$ | $u_g/u_{max}$ | $L_d$ (mm) |
|--------|---------------|------------|
| 325    | 0.667         | 17         |
| 810    | 0.721         | 42         |
| 1065   | 0.723         | 50         |
| 1190   | 0.757         | 55         |

540 on the presumption that air enters the channel with a uniform velocity profile and using  
 541 the Blasius correlation, it is straightforward to show that:

$$\frac{L_d}{H} = 0.01 Re_g \quad (\text{A } 2)$$

542 Based on this data, it is clear that the gas flow is fully developed in the entire region  
 543 of the channel used for our falling liquid film experiments.

544 A specific velocity measurement series has been performed to confirm the laminar-  
 545 turbulent transition threshold determined by Patel & Head (1969). The top glass plate  
 546 of the channel was replaced by a Plexiglas plate with an opening to allow access for the  
 547 probe far from the air entrance (about 1 m away). In this campaign, only the maximum  
 548 air velocity,  $u_{max}$ , has been measured for different fan powers. By assuming that the flow  
 549 is laminar and fully-developed at this location, i.e.  $u_g \approx 0.667u_{max}$ , we can calculate a  
 550 flow rate and then a Reynolds number,  $Re_g^{lam}$ . For a given fan power, we compare  $Re_g^{lam}$   
 551 with  $Re_g$  issued from the complete vertical velocity profiles (using (A 1) then (2.3)).  
 552 Figure 20 displays  $Re_g^{lam}$  and  $Re_g$  against the imposed fan power. It can be seen that  
 553 for  $Re_g \leq 1200$  the points collapse, which means that  $Re_g = Re_g^{lam}$  and thus the flow is  
 554 confirmed to be laminar. The discrepancy observed for  $Re_g > 1200$  means that the flow  
 555 is no longer laminar. From these measurements we can conclude that in our inclined  
 556 channel, the laminar-turbulent transition occurs for  $Re_g$  slightly greater than 1200.

557 The gas Reynolds number,  $Re_g$ , defined in (2.3) can be used to characterize the counter-  
 558 current air flow in the experiments provided that the gas flow rate circulating into the

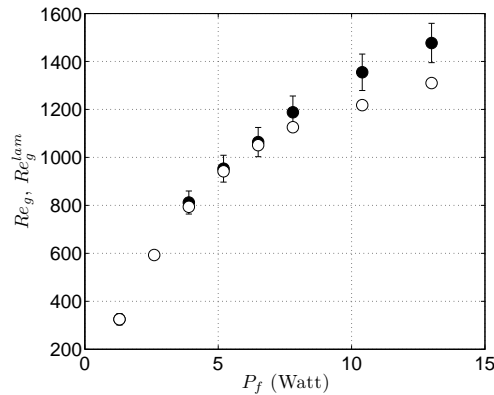


Figure 20:  $Re_g$  (filled circles) and  $Re_g^{lam}$  (open circles) as a function of the fan power  $P_f$ .  $Re_g$  is calculated by integrating velocity profiles measured at the end of the channel (figure 18), and  $Re_g^{lam}$  from the maximum velocity measurements performed in the fully-developed region and assuming a laminar parabolic profile i.e.  $u_g = 2/3u_{max}$ .

559 experimental gas loop is not affected by the presence of the liquid film in the channel at  
 560 a fixed fan power. The validity of this assumption is discussed below.

561 For a gas flowing in a dry rectangular channel with a large transversal aspect ratio  
 562 of length  $L$  and height  $H$  (in our configuration  $W/H = 54 \gg 1$ ), the pressure drop  
 563 is given by the analytic relation  $\Delta p_{channel} = 4C_f \frac{L}{2H} \frac{1}{2} \rho_g (\frac{q}{H})^2$  where  $q = u_g H$  is the  
 564 volumetric gas flow rate (per unit width, i.e.  $q = q_g/W$ ) and  $C_f$  is the skin friction  
 565 coefficient, with  $C_f = 12/Re_g$ . Thus,  $\Delta p_{channel} \propto q/H^3$  and the corresponding power  
 566  $P_{channel} = q \Delta p_{channel} \propto q^2/H^3$ . For a given power value  $P_{channel}$ , decreasing the channel  
 567 height by 10% (typical to the reduction due to the presence of the liquid film in the  
 568 experiments) leads to a 15% decrease in the flow rate. However,  $\Delta p_{channel}$  constitutes  
 569 only a small part of the total pressure drop, which is dominated by the resistance in  
 570 the section between the outlet slot and the fan. Thus, the actual decrease in  $q_g$  upon  
 571 decreasing  $H$  by 10% is relatively low. For the range of parameters considered in this  
 572 study, we have estimated it to be less than 5%.



## 573 Appendix B. Flat-film model for laminar and turbulent gas flow

574 In panel 16b, we have estimated the liquid film thickness of the flat-surface primary  
 575 flow based on the skin friction coefficient  $C_{f,i}$ . This approach allows to account for a  
 576 laminar or turbulent gas flow within the flat-film model. For laminar flow, this coefficient  
 577  $C_{f,i}$  is given by (3.9) and for turbulent flow by (3.10), according to the experiments of  
 578 Patel & Head (1969). However, these experiments were performed in a dry channel, and,  
 579 thus, our flat-film model implies an immobile liquid-gas interface. The current appendix  
 580 aims to verify this assumption. We do this based on the laminar case, which is the limiting  
 581 one, and for which we can easily obtain a reference solution for the flat-surface film based  
 582 on the fully-coupled primary flow (Lavalle *et al.* 2019).

583 The gas velocity profile for the fully-coupled primary flow is given by:

$$u(Y) = \frac{-K_g}{2\mu_g} H_g^2 (Y - Y^2) + u_0 (1 - Y), \quad (\text{B1})$$

584 where  $K_g$  reads:

$$K_g = \left( \partial_x p - \rho_g g \sin \beta \right), \quad (\text{B2})$$

585 where  $\partial_x p$  is the driving longitudinal pressure gradient, positive in our case for a counter-  
 586 current gas flow, and  $Y = (y - h_{flat})/H_g$ , with  $h_{flat}$  denoting the flat-surface film  
 587 thickness and  $H_g = H - h_{flat}$  the height of the gas cross-section.  $u_0$  is the liquid velocity  
 588 at the film surface ( $u_0 > 0$ ).

589 The gas velocity averaged over  $H_g$  can be written as:

$$u_g^+ = \frac{-K_g}{12\mu_g} H_g^2 + \frac{u_0}{2} = u_g^0 + \frac{u_0}{2} = u_g^0 \left( 1 + \frac{\epsilon}{2} \right), \quad (\text{B3})$$

590 where  $u_g^0$  corresponds to the average gas velocity in the limit  $u_0 = 0$  and  $\epsilon = u_0/u_g^0$ .

591 The gas Reynolds number is defined as:

$$Re_g^+ = \frac{u_g^+ H_g}{\nu_g} = \frac{u_g^0 H_g}{\nu_g} + \frac{u_0 H_g}{2\nu_g} = Re_g^0 + Re_0 = Re_g^0 \left( 1 + \frac{\epsilon}{2} \right) \quad (\text{B4})$$

592 We can write the tangential shear-stress at the liquid-gas interface and at the top wall,  
 593  $\tau_i$  and  $\tau_w$ , as:

$$\tau_i = -\frac{\mu_g}{H_g} \partial_Y u|_{Y=0} = \frac{K_g}{2} H_g + \mu_g \frac{u_0}{H_g} = \tau_i^0 \left( 1 - \frac{\epsilon}{6} \right), \quad (\text{B5})$$

$$\tau_w = \frac{\mu_g}{H_g} \partial_Y u|_{Y=1} = \frac{K_g}{2} H_g - \mu_g \frac{u_0}{H_g} = \tau_i^0 \left( 1 + \frac{\epsilon}{6} \right), \quad (\text{B6})$$

594 where  $\tau_i^0 = H_g K_g/2$  is the limit of  $\tau_i$  and  $\tau_w$  for a static interface (i.e. for  $\epsilon = 0$ ).

595 We define the global skin-friction coefficient at the liquid-gas interface,  $C_{f,i}$  as:

$$\begin{aligned} C_{f,i} &= \frac{\tau_i}{1/2\rho_g u_g^{+2}} \\ &= \frac{\tau_i^0}{1/2\rho_g u_g^{02}} \frac{1 - \epsilon/6}{(1 + \epsilon/2)^2} = C_{f,i}^0 \frac{1 - \epsilon/6}{(1 + \epsilon/2)^2} \end{aligned} \quad (\text{B7})$$

596 In a similar way we can define  $C_{f,w}$  at the top wall as:

$$C_{f,w} = C_{f,i}^0 \frac{1 + \epsilon/6}{(1 + \epsilon/2)^2} \quad (\text{B8})$$

597  $C_{f,i}^0$  is the skin friction coefficient in the case of static boundaries (i.e. for  $\epsilon = 0$ ). In

24

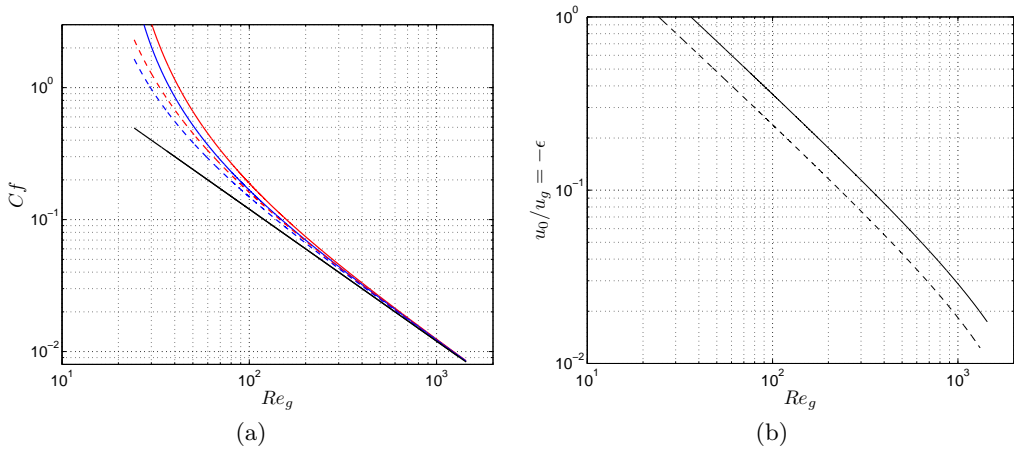


Figure 21: (a) Global skin-friction coefficients at the liquid-gas interface  $C_{f,i}$  (B 7) (red line) and at the upper wall of the channel  $C_{f,w}$  (B 8) (blue line) as a function of  $Re_g$ , calculated from the fully-coupled primary flow solution. The black line corresponds to a skin-friction coefficient in the case of a static interface (i.e.  $\epsilon = 0$ ). (b) Ratio between the interface velocity and the gas velocity  $u_0/u_g = -\epsilon$ .  $Re_l = 22$  (dashed lines) and  $Re_l = 44.6$  (solid lines),  $\beta = 4.9^\circ$ ,  $H = 5.2$  mm.

598 the case of a laminar gas flow, it is given by:

$$C_{f,i}^0 = \frac{-12}{Re_g^0} \quad (\text{B 9})$$

599 For convenience, in the experiments  $u_g$  is always taken as positive, therefore  $u_g = -u_0^0$   
 600 and  $Re_g = -Re_g^0$  in our counter-current case.

601 Now, we compute  $C_{f,i}$  and  $C_{f,w}$  based on (B 7) and (B 8), using the liquid velocity at  
 602 the interface  $u_0$  (which enters  $\epsilon$ ) from the fully-coupled primary-flow solution. Figure 21a  
 603 displays  $C_{f,i}$  (red lines),  $C_{f,w}$  (blue lines) and  $C_{f,i}^0$  (black line) as a function of the gas  
 604 Reynolds number  $Re_g = -Re_g^0$  over the range  $25 < Re_g < 1500$ , for two liquid Reynolds  
 605 numbers considered in our experiments with  $H = 5.2$  mm:  $Re_l = 22$  (dashed lines) and  
 606  $Re_l = 44.6$  (solid lines). The associated variation of  $u_0/u_g = -\epsilon$  is presented in figure 21b.  
 607 To specify the range of parameters where the static interface approximation based on the  
 608 skin-friction coefficient criteria can be considered as valid, we focus on the gas Reynolds  
 609 values such as the difference between  $C_{f,i}$  and  $C_{f,i}^0$  is less than 10%. From figure 21a  
 610 we can conclude that this criterion is met for  $Re_g > 250$  ( $Re_l = 22$ ) and  $Re_g > 400$   
 611 ( $Re_l = 44.6$ ), which corresponds to  $u_0/u_g \leq 0.08$  in figure 21b. Figure 21a also shows  
 612 that  $C_{f,i} \approx C_{f,w}$  over a range of  $u_0/u_g$  where the static interface assumption is no longer  
 613 valid. For example the discrepancy between  $C_{f,i}$  and  $C_{f,w}$  is around 10% in figure 21a for  
 614  $(Re_l, Re_g) = (22, 80)$  and  $(44.6, 125)$ , corresponding to  $u_0/u_g \approx 0.3$  in figure 21b. This  
 615 behaviour can be explained by the change in the the gas velocity distribution with the  
 616 gas flow rate. Indeed, the location of the maximum gas velocity is shifted towards the  
 617 top wall when  $u_0/u_g$  is increased by decreasing  $Re_g$ , as shown in figure 22. Consequently,  
 618 the tangential shear stress is reduced at the liquid/gas interface while it increases at the  
 619 top wall and the dissymetry arising from the moving interface is partially attenuated.

620 To go further in testing the validity of this frozen-interface approximation, we will  
 621 compare the film thickness obtained from the fully-coupled primary flow solution with

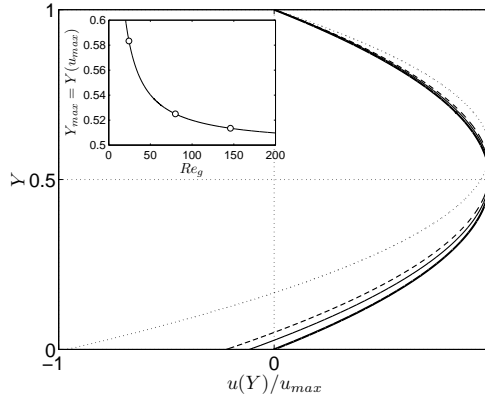


Figure 22: Gas velocity profiles calculated from the fully-coupled primary flow solution for  $Re_l = 22$ :  $u(Y)/u_{max}$  with  $u(Y)$  according to (B 1) and  $u_{max} = \min(u(Y)) < 0$ . Dash-dot line,  $u_0/u_g = 1$  ( $Re_g = 24.3$ ); dashed line,  $u_0/u_g = 0.3$  ( $Re_g = 80$ ); solid line,  $u_0/u_g = 0.16$  ( $Re_g = 145$ ); thick solid line,  $u_0 = 0$  (Poiseuille flow). The location of  $u_{max}$  in the channel,  $Y_{max} = Y(u_{max})$ , is plotted in the inset as a function of  $Re_g$  ( $Y_{max} = 0.5$  for a Poiseuille flow). Open circles mark  $Y_{max}$  for the profiles represented in the figure (except the Poiseuille flow).  $\beta = 4.9^\circ$ ,  $H = 5.2$  mm.

622 the thickness obtained by assuming an inter-phase skin friction coefficient according to  
623 (B 9) using a simple model described below.

624 We start by writing the velocity profile in the liquid film:

$$u_l(y) = \frac{K_l}{\mu_l} \left( h_{flat} y - \frac{y^2}{2} \right) - \frac{\tau_i}{\mu_l} y \quad (\text{B } 10)$$

625  $K_l$  reads:

$$K_l = \left( (\rho_l - \rho_g) g \sin \beta - \frac{\tau_i + \tau_w}{H - h_{flat}} \right), \quad (\text{B } 11)$$

626 where  $\tau_i$  and  $\tau_w$  are given by (B 5) and (B 6), respectively. Therefore,  $\tau_i + \tau_w = 2\tau_i^0 =$   
627  $\rho_g u_g^0 C_{f,i}^0 = \rho_g u_g^0 C_{f,i}^0$ .

628 Integrating (B 10) across the liquid layer gives the liquid flow rate:

$$Q_l = \frac{K_l}{3\mu_l} h_{flat}^3 - \frac{\tau_i}{2\mu_l} h_{flat}^2 \quad (\text{B } 12)$$

629 By expressing the flowrate  $Q_l = (\rho_l g \sin \beta) (3\mu_l)^{-1} h_N^3$  in terms of the Nusselt thickness  
630  $h_N$ , i.e. the thickness of an equivalent fully-developed flat-surface film falling in a passive  
631 atmosphere, we obtain the following equation for the flat-surface film thickness sheared  
632 by a counter-current gas flow:

$$\left( 1 - \frac{\rho_g}{\rho_l} - \underbrace{Fr_{g,l}^2 C_{f,i}^0 \left( \frac{H}{h_N} - \tilde{h}_{flat} \right)^{-1}}_{\Lambda_p} \right) \tilde{h}_{flat}^3 - \underbrace{\frac{3}{4} Fr_{g,l}^2 C_{f,i}^0 (1 - \epsilon/6) \tilde{h}_{flat}^2 - 1}_{\Lambda_i} = 0, \quad (\text{B } 13)$$

633 where  $\tilde{h}_{flat} = h_{flat}/h_N$ . The contribution of pressure gradient in the gas phase is included  
634 in  $\Lambda_p$  and the contribution of the interfacial shear-stress is included in  $\Lambda_i$ . The inter-phase

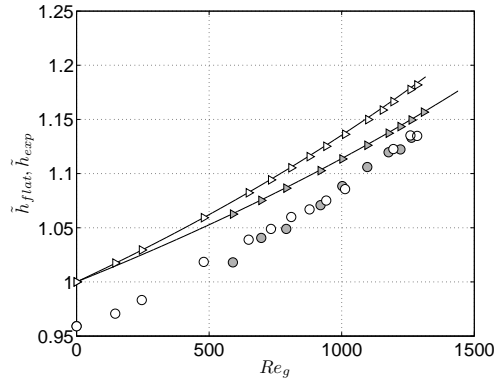


Figure 23: Thickness of a flat-surface film (normalized by the Nusselt thickness  $h_N$ ) subject to a counter-current laminar gas flow, obtained from the flat-film model (triangles) (according to (B 13) with  $\epsilon = 0$ ) compared with the numerical solution of the fully-coupled two-phase primary flow (solid lines). The normalized mean film thickness  $\tilde{h}_{exp} = h_m/h_N$  measured in the experiments is also reported (circles).  $Re_l = 22$  (white symbols) and  $Re_l = 44.6$  (grey symbols),  $\beta = 4.9^\circ$ ,  $H = 5.2$  mm.

635 skin friction coefficient  $C_{f,i}^0$  is given by (B 9) in the laminar case and  $Fr_{g,l}$  is given by  
 636 (3.4).

637 The contribution of the moving interface is represented by  $\epsilon = u_0/u_g^0$ , the ratio between  
 638 the interface velocity and the gas velocity ( $\epsilon < 0$  in our counter-current case). By  
 639 assuming  $\epsilon = 0$ , i.e. the liquid/gas interface is static, the liquid and gas phases are  
 640 coupled only via the interface position  $h_{flat}$ .

641 In figure 23, we compare the solution given by the model from solving (B 13) assuming  
 642  $\epsilon = 0$  (symbols) with the film thickness obtained from solving the fully-coupled two-phase  
 643 primary flow (solid lines), for  $Re_l = 22$  and  $Re_l = 44.6$ , and for gas Reynolds number  
 644 values according to the experiments. The results obtained from these two approaches are  
 645 in excellent agreement over the entire range of experimental conditions, even for small  
 646 gas Reynolds numbers for which  $|\epsilon|$  is not so small. Indeed, if we go back for example to  
 647 the aforementioned experiment conducted with  $Re_l = 22$  and  $Re_g = 145$ ,  $\epsilon = -0.3$  (see  
 648 figure 21b) which implies that the effect of the interfacial shear stress ( $\Lambda_i$  in (B 13)) is  
 649 underestimated by only  $0.3/6 = 5\%$  by assuming an immobile liquid/gas interface. From  
 650 this analysis, we can conclude that this approximation is admissible in all the experiments  
 651 presented in the current paper.

652 Finally, the normalized mean film thickness  $\tilde{h}_{exp} = h_m/h_N$  measured in the experi-  
 653 ments is also reported in figure 23, for  $Re_l = 22$  and  $Re_l = 44.6$ . We observe that  
 654  $\tilde{h}_{exp} < \tilde{h}_{flat}$  reflecting the effective film thinning due to the presence of interfacial waves  
 655 in experiments. For  $Re_l = 22$ ,  $\tilde{h}_{exp}$  increases in the same amount as  $\tilde{h}_{flat}$  when the gas  
 656 flow is increased, whereas  $\tilde{h}_{exp}$  increases faster than  $\tilde{h}_{flat}$  for  $Re_l = 44.6$ . This behaviour  
 657 is discussed in §3.3.

## REFERENCES

- 658 ALEKSEENKO, S.V., AKTERSHEV, S.P., CHERDANTSEV, A.V., KHARLAMOV, S.M. &  
 659 MARKOVICH, D.M. 2009 Primary instabilities of liquid film flow sheared by turbulent  
 660 gas stream. *Int. J. of Multiphase Flow* **35**, 617–627.

- 661 BENJAMIN, T. BROOKE 1957 Wave formation in laminar flow down an inclined plane. *J. Fluid*  
662 *Mech.* **2**, 554–574.
- 663 COHEN-SABBAN, J., GAILLARD-GROLEAS, J. & CREPIN, P.-J. 2001 Quasi-confocal extended  
664 field surface sensing. *Proceedings of SPIE, Optical Metrology Roadmap for Semiconductor,*  
665 *Optical, and Data Storage Industries II* **4449**, 178–183.
- 666 DIETZE, GEORG F. 2016 On the Kapitza instability and the generation of capillary waves.  
667 *J. Fluid Mech.* **789**, 368–401.
- 668 DIETZE, GEORG F. & RUYER-QUIL, CHRISTIAN 2013 Wavy liquid films in interaction with a  
669 confined laminar gas flow. *J. Fluid Mech.* **722**, 348–393.
- 670 DROSOS, E.I.P., PARAS, S.V. & KARABELAS, A.J. 2006 Counter-current gas–liquid flow in a  
671 vertical narrow channel - Liquid film characteristics and flooding phenomena. *Int. J. of*  
672 *Multiphase Flow* **32** (1), 51–81.
- 673 KAPITZA, P. L. 1948 Wave flow of a thin viscous fluid layers. *Zh. Eksp. Teor. Fiz.* **18**.
- 674 KOFMAN, N., MERGUI, S. & RUYER-QUIL, C. 2017 Characteristics of solitary waves on a falling  
675 liquid film sheared by a turbulent counter-current gas flow. *Int. J. of Multiphase Flow* **95**,  
676 22–34.
- 677 KUSHNIR, R., BARMAK, I., ULLMANN, A. & BRAUNER, N. 2021 Stability of gravity-driven  
678 thin-film flow in presence of an adjacent gas phase. *Int. J. of Multiphase Flow* **135**, 1–17.
- 679 LAVALLE, G., GRENIER, N., MERGUI, S. & DIETZE, G. F. 2020 Solitary waves on superconfined  
680 falling liquid films. *Phys. Rev. Fluids* **5** (3), 032001(R).
- 681 LAVALLE, G., LI, Y., MERGUI, S., GRENIER, N. & DIETZE, G. F. 2019 Suppression of the  
682 kapitza instability in confined falling liquid films. *J. Fluid Mech.* **860**, 608–639.
- 683 LAVALLE, G., MERGUI, S., GRENIER, N. & DIETZE, G. 2021 Superconfined falling liquid films  
684 : linear versus nonlinear dynamics. *J. Fluid Mech.* **919**, R2.
- 685 LIU, J. & GOLLUB, J.P. 1994 Solitary wave dynamics of film flows. *Physics of Fluids* **6** (5),  
686 1702.
- 687 LIU, J., PAUL, J.D. & GOLLUB, J. P. 1993 Measurements of the primary instabilities of film  
688 flows. *J. Fluid Mech.* **250**, 69–101.
- 689 MIYARA, A. 1999 Numerical analysis on flow dynamics and heat transfer of falling liquid films  
690 with interfacial waves. *Heat and Mass Transfer* **35**, 298–306.
- 691 PATEL, V.C. & HEAD, M.R. 1969 Some observations on skin friction and velocity profiles in  
692 fully developed pipe and channel flows. *J. Fluid Mech.* **38** (1), 181–201.
- 693 TILLEY, B. S., DAVIS, S. H. & BANKOFF, S. G. 1994 Nonlinear long-wave stability of superposed  
694 fluids in an inclined channel. *J. Fluid Mech.* **277**, 55–83.
- 695 TRIFONOV, Y Y 2010 Counter-current gas-liquid wavy film flow between the vertical plates  
696 analyzed using the Navier-Stokes equations. *AIChE Journal* **56** (8), 1975–1987.
- 697 TRIFONOV, Y. Y. 2017 Instabilities of a gas-liquid flow between two inclined plates analyzed  
698 using the navier–stokes equations. *Int. J. Multiph. Flow* **95**, 144 – 154.
- 699 TRIFONOV, Y. Y. 2019 Nonlinear wavy regimes of a gas-liquid flow between two inclined plates  
700 analyzed using the navier–stokes equations. *Int. J. Multiph. Flow* **112**, 170 – 182.
- 701 TSELUIKO, D. & KALLIADASIS, S. 2011 Nonlinear waves in counter-current gas-liquid film flow.  
702 *J. Fluid Mech.* **673**, 19–59.
- 703 VALLURI, P., MATAR, O. K., HEWITT, G.F. & MENDES, M.A. 2005 Thin film flow over  
704 structured packings at moderate Reynolds numbers. *Chem. Eng. Sc.* **60**, 1965–1975.
- 705 VELLINGIRI, R., TSELUIKO, D. & KALLIADASIS, S. 2015 Absolute and convective instabilities  
706 in counter-current gas–liquid film flows. *J. Fluid Mech.* **763**, 166–201.
- 707 VLACHOS, N. A., PARS, S. V., MOUZA, A. A. & KARABELAS, A. J. 2001 Visual observations  
708 of flooding in narrow rectangular channels. *Int. J. of Multiphase Flow* **27**, 1415–1430.
- 709 YIH, C. S. 1963 Stability of Liquid Flow down an Inclined Plane. *Phys. Fluids* **6** (3), 321–334.
- 710 ZAPKE, A. & KRÖGER, D.G. 2000 Counter-current gas-liquid flow in inclined and vertical ducts  
711 - i: Flow patterns, pressure drop characteristics and flooding. *Int. J. of Multiphase Flow*  
712 **26**, 1439–1455.